

Pinky Chowdhury

# **3D PRINTING OF BIOPHOTONIC SCAFFOLD WITH LONG LASTING GREEN EMISSION AF- TER NIR CHARGING**

Master of Science Thesis  
Faculty of Engineering and Natural Sciences  
Examiner: Dr. Nirajan Ojha  
Dr. Virginia Alessandra Gobbo  
Prof. Dr. Laeticia Petit  
November, 2025

# ABSTRACT

Pinky Chowdhury: 3D Printed Biophotonic Scaffold With Long Lasting Emission After NIR Charging.  
Master Thesis  
Tampere University  
Photonics Technologies  
October 2025

---

Blue upconverter (UC) crystals, when incorporated into biophotonic scaffolds, can present a promising approach for biomedical applications like drug release, tissue regeneration.

In this work,  $\text{CaWO}_4$ : ( $\text{Yb}^{3+}/\text{Tm}^{3+}/\text{Nd}^{3+}$ ) crystals, prepared using a solid-state reaction, were found to emit blue light under 808nm and 980nm excitation. The role of  $\text{Nd}^{3+}$  in this emission is discussed. The blue emission intensity from  $\text{Tm}^{3+}$  in  $\text{Yb}^{3+}/\text{Tm}^{3+}/\text{Nd}^{3+}$  triply doped  $\text{CaWO}_4$  under 808 nm pumping was achieved through  $\text{Nd}^{3+}$  sensitization with  $\text{Yb}^{3+}$  ions, facilitating energy transfer, whereas the blue emission under 980nm was only due to  $\text{Yb}^{3+}$  activating  $\text{Tm}^{3+}$ . The UC crystals-Persistent Luminescent (PeL) phosphors ratio was optimized to achieve the best optical performance: long-lasting green emission after 808 and 980 nm charging. The porous biophotonic scaffold, fabricated using the robocasting method, consisted of UC crystal, PeL phosphor  $\text{SrAl}_2\text{O}_4$ :  $\text{Eu}^{2+}$ ,  $\text{Dy}^{3+}$ , and bioactive glass 1393B20. The printability of the scaffolds by using a 3D printer is also discussed. Upon 808nm excitation, scaffolds lose their green afterglow but still emit blue emission. However, at 980nm, it shows intense blue emission with strong green afterglow.

Here, the challenges related to the fabrication of these composites are discussed. The elevation of sample temperature influenced by laser irradiation is suspected to depend on the doping concentration of  $\text{Nd}^{3+}$  and the excitation power density of the 808nm pump laser.

The printability of the composite ink into biophotonic scaffolds has been proven, opening a new perspective in smart photoactivable materials for photo-induced drug release within bone tissue engineering.

**Keywords:** 3D printing, scaffold, bioactive glass, persistent luminescence, blue upconversion, green afterglow, rare-earth ions, XRD

The originality of this thesis has been verified using the Turnitin Originality Check service.

## USE OF AI IN THESIS

I have utilized AI tools in my thesis:

- No
- Yes

The AI tools utilized in my thesis and their purposes are described below:

Names and versions of AI tools: Chat GPT Version 5

Purpose of using AI tools: See the grammatical structure, sentence formation, and paraphrase the sentence.

I acknowledge that I am fully responsible for the entire content of my thesis, including the parts generated by AI, and accept accountability for any violations of ethical standards in publications.

# **PREFACE**

This master's thesis has been carried out at the Photonic Glass Group (PGG), Tampere University, Finland. First, I would like to thank my supervisor, Dr. Nirajan Ojha, and Dr. Virginia Alessandra Gobbo, for their tremendous teaching, support, and help. They always responded to all my confusions and questions. I would like to thank my co-supervisor, Professor Laetitia Petit, for her guidance and constant support throughout the project.

Also, I want to thank my friends Amna, Arjun, Redwan, and Zubair for their continuous support throughout my whole master's period and thesis work.

I am so grateful to my course co-ordinator, Tea Velloma, for her selfless help and support from the very beginning of my studies in Photonics Technologies. Finally, I would like to extend special thanks to my parents, Mr. & Mrs. Chowdhury, spouse Apu, and my only beloved son, Praggo Ayangshu, for their support and cooperation.

Tampere, November 2025

Pinky Chowdhury (TAU)

# CONTENT

LIST OF FIGURES.....	V
LIST OF TABLES.....	VII
INTRODUCTION.....	1
CHAPTER 1: BACKGROUND.....	3
1.1 Bioactive Glass .....	3
1.1.1 <i>Bioactive Glass and Its Properties</i> .....	3
1.1.2 <i>Bioactive Scaffold and Its Properties</i> .....	5
1.1.3 <i>Fabrication of 3D Scaffold</i> .....	7
1.2 Luminescent Materials .....	9
1.2.1 <i>Rare Earth ions</i> .....	9
1.2.2 <i>Upconversion Process</i> .....	11
1.2.3 <i>Persistent Luminescence (PeL) Process</i> .....	13
1.3 Applications of 3D Printed Scaffold .....	15
1.3.1 <i>Green Light Use of Prevent Infection</i> .....	15
1.3.2 <i>Excitation Using 808 nm and 980 nm</i> .....	15
CHAPTER 2: EXPERIMENTAL PART .....	17
2.1 Bioactive Scaffold Preparation .....	17
2.1.1 <i>Glass Melting</i> .....	17
2.1.2 <i>Crystal Synthesis</i> .....	18
2.1.3 <i>3D Printing</i> .....	18
2.2.XRD Analysis .....	21
2.3 Spectroscopic Properties .....	22
CHAPTER 3: RESULTS AND DISCUSSION .....	24
3.1 Crystal Synthesis and Characterization .....	24
3.1.1 <i>YPO<sub>4</sub> and CaWO<sub>4</sub> (Nd<sup>3+</sup>, Tm<sup>3+</sup>)</i> .....	24
3.1.2 <i>CaWO<sub>4</sub> (Yb<sup>3+</sup>, Tm<sup>3+</sup>)</i> .....	26
3.1.3 <i>CaWO<sub>4</sub> (Yb<sup>3+</sup>, Tm<sup>3+</sup>, Nd<sup>3+</sup>)</i> .....	28
3.2 3D printing of Scaffolds .....	29
3.2.1 <i>UC-PeL ratio optimization</i> .....	29
3.2.2 <i>3D Printed Scaffolds and Characterization</i> .....	32
CONCLUSIONS.....	36
REFERENCES.....	38

# LIST OF FIGURES

Figure 1.	Different types of bioactive glass with different methods (Fagerlund,12) .....	3
Figure 2.	SME image of cross section S53P4 (A) and 1393B20 (B) conditioned and analyzed by EDX, scale bar 20 $\mu\text{m}$ (Deraine,21) .....	4
Figure 3.	Mircostructures of bioactive glass scaffolds made using various techniques (Rahaman, 11) .....	6
Figure 4.	Algorithm for the development of an osteoconstructive porous Ti bioimplant (Kiselevskiy,23).....	6
Figure 5.	Schematics of different types of 3D printing (Kaur,25).....	7
Figure 6.	Period table of the rare earth elements (E-tech resources,21) .....	9
Figure 7.	Separated RE extract oxides from solvent extraction (Shin-Etsu RE) .....	10
Figure 8.	Properties and Characteristics of the RE elements (Prajzler,10) .....	11
Figure 9.	Simplified energy level diagrams describing up-conversion processes: (a) ESA, (b) ETU, (c) PA, (d) CUC, and (e) EMU (red: excitation; blue: UC emission, green: energy transfer)(Thirumalai, 16).....	12
Figure 10.	Three-color persistent luminescence panel based on the $\text{Sr}_2\text{MgSi}_2\text{O}_7:\text{Eu}^{2+}, \text{Dy}^{3+}$ (blue), $\text{SrAl}_2\text{O}_4:\text{Eu}^{2+}, \text{Dy}^{3+}$ (green), and $\text{Y}_2\text{O}_2\text{S}:\text{Eu}^{3+}, \text{Mg}^{2+}, \text{Ti}$ (red) phosphors (Brito,12).....	14
Figure 11.	Schematic diagram of a persistent luminescence mechanism under band-to-band (Xu,19) .....	14
Figure 12.	(a) Laser light pattern 808 nm at 3.3 cm tissue depth, (b) Laser light pattern 980 nm at 2.8 cm tissue depth (Hudson,13) .....	16
Figure 13.	Picture of furnaces used for glass melting and annealing.....	17
Figure 14.	As-prepared Pluronic® F-127 aqueous solution.....	19
Figure 15.	Image of the 3D printing process with 5 wt% UC-10 wt% PeL mix. ....	20
Figure 16.	Visible green PeL in the ink.....	20
Figure 17.	Schematic representation of Bragg's equation (Stan,18).....	21
Figure 18.	Schematic diagram of powder XRD .....	22
Figure 19.	Experimental setup of UC emission .....	23
Figure 20.	Energy level diagrams of Tm, Yb, Nd ions and the possible UC under 808 nm excitation (Tian,20).....	23
Figure 21.	. (a) XRD patterns of the $\text{Y}_{(1-x-y)}\text{PO}_4\text{Nd}_x\text{Tm}_y$ crystals with different amount of $\text{Nd}_2\text{O}_3$ and 0.5at% of $\text{Tm}_2\text{O}_3$ ; (b) XRD of the $\text{Ca}_{1-x-y-z}\text{WO}_4\text{Nd}_x\text{Tm}_y\text{Na}_z$ crystals with different amount of $\text{Nd}_2\text{O}_3$ and 0.5at% of $\text{Tm}_2\text{O}_3$ .....	25
Figure 22.	$\text{Ca}_{1-2(x+y)}\text{WO}_4\text{Nd}_x\text{Tm}_y\text{Na}_{(x+y)}$ crystal (Nd 20at.%) difficult to extract.....	25
Figure 23.	No upconversion at 808nm excitation codoped with $\text{Nd}^{3+}/\text{Tm}^{3+}$ ions (a) $\text{Y}_{(1-x-y)}\text{PO}_4\text{Nd}_x\text{Tm}_y$ crystals, (b) $\text{Ca}_{1-2(x+y)}\text{WO}_4\text{Nd}_x\text{Tm}_y\text{Na}_{(x+y)}$ crystals .....	26
Figure 24.	(a) XRD patterns of $\text{Ca}_{1-2(x+y)}\text{WO}_4\text{Yb}_x\text{Tm}_y\text{Na}_{(x+y)}$ crystals prepared with different amounts of $\text{Yb}_2\text{O}_3$ and 0.25 at% of $\text{Tm}_2\text{O}_3$ ; (b) XRD patterns of $\text{Ca}_{1-2(x+y)}\text{WO}_4\text{Yb}_x\text{Tm}_y\text{Na}_{(x+y)}$ crystals with 7.5 at% $\text{Yb}_2\text{O}_3$ and different amounts of $\text{Tm}_2\text{O}_3$ .....	26
Figure 25.	(a) Normalized upconversion spectrum of $\text{Yb}_x7.5\text{Tm}_y0.25$ crystal, taken as an example. (b) Relative intensity of the blue emission at 475 nm as a function of $\text{Yb}_2\text{O}_3$ at%(x) and $\text{Tm}_2\text{O}_3$ at%(y) in the crystals ( $\lambda_{\text{exc}} = 808\text{nm}$ ) .....	27
Figure 26.	XRD patterns of the $\text{Ca}_{1-2(x+y)-z}\text{WO}_4\text{Yb}_x\text{Tm}_y\text{Nd}_z\text{Na}_{(x+y)}$ with different amounts of $\text{Nd}_2\text{O}_3$ with 10 at% $\text{Yb}_2\text{O}_3$ & 0.25 at% $\text{Tm}_2\text{O}_3$ .....	28

Figure 27.	(a) Normalized UC spectrum of the $\text{Yb}_x\text{10}, \text{Tm}_y\text{0.25}, \text{Nd}_z(0 \text{ to } 2)$ at% crystal $\text{Ca}_{1-2(x+y)-z}\text{WO}_4\text{Yb}_x\text{Tm}_y\text{Nd}_z\text{Na}_{(x+y)}$ , (b) relative intensity of the blue emission at 475nm as a function of $\text{Nd}_2\text{O}_3$ at% in the crystals ( $\lambda_{\text{exc}} = 808\text{nm}$ ).....	29
Figure 28.	Intensity of UC-PeL crystals without $\text{Nd}^{3+}$ different concentrations of UC crystal and PeL (a) in 808 nm laser pump with weak afterglow; (b) in 980 nm laser pump, strong green afterglow.....	30
Figure 29.	Intensity of UC-PeL crystals with $\text{Nd}^{3+}$ different concentrations of UC & PeL (a) in 808 nm (b) in 980 nm excitation .....	31
Figure 30.	Picture of unsintered and sintered scaffolds without $\text{Nd}^{3+}$ in daylight, and after UV charging .....	32
Figure 31.	XRD patterns of sintered-unsintered scaffold and 1393B20 glass powder.....	33
Figure 32.	Relative Intensity of Sintered and Unsintered scaffold without $\text{Nd}^{3+}$ doped crystal (a) in 808 nm excitation (b) in 980 nm excitation .....	33
Figure 33.	Pictures of Sintered and Unsintered scaffolds in daylight and after UV charging .....	34
Figure 34.	Relative Intensity of Sintered and Unsintered Scaffold with $\text{Yb}^{3+}/\text{Tm}^{3+}/\text{Nd}^{3+}$ doped crystal (a) in 808nm (b) in 980nm .....	35

# LIST OF TABLES

<i>Table 1 Nominal Glass Composition (mol%)</i> .....	18
<i>Table 2. Composition of UC-PeL Glass Powder</i> .....	19

# LIST OF SYMBOLS AND ABBREVIATIONS

$\lambda$ (lenda)	Wavelength
$\theta$ (theta)	Diffraction Angle
at%	Atomic Percentage
wt%	Weight Percentage
$\mu\text{m}$	Micrometer
nm	Nanometer
2PL	Two Photon Lithography
3D	Three Dimensional
AM	Additive Manufacturing
BAG	Bioactive Glass
C <sub>2</sub> C <sub>12</sub>	Murine Myoblastic cell line
CDT	Chemo Dynamic Therapy
CIJ	Continuous Inkjet
CUC	Cooperative Upconversion
d	Interplane spacing in Bragg's law
EDX	Energy Dispersive X-Ray Spectroscopy
EMU	Energy Migration Upconversion
ESA	Excited State Absorption
ETU	Energy Transfer Upconversion
FDM	Fused Deposition Modeling
FFF	Fused Filament Fabrication
FTIR	Fourier Transform Infrared Spectroscopy
DIW	Direct Ink Writing
DOD	Drop On Demand
DLP	Digital Light Processing
HA	Hydroxyapatite
hADSCs	Human Adipose-Derived Stem Cell
hBMSCs	Human Bone-Marrow-Derived Mesenchymal Stem Cell
LAB	Laser Assisted Bioprinting
MC3T3-E1	Murine Pre-Osteoblastic Cell Line
NIR	Near Infrared
PA	Photon Avalanche
PB	Particle Binding
PeL	Persistent Luminescence
PLA	Polylactic Acid
PLNPs	Persistent Luminescence Nano Particles
PDT	Photo Dynamic Therapy
PTT	Photo Thermal Therapy
RE	Rare Earth
RE <sup>+</sup>	Rare Earth ions
sHA	Synthetic Hydroxyapatite
SDT	Sono Dynamic Therapy
SEM	Scanning Electron Microscopy
SLA	Stereolithography
SLS	Selective Laser Sintering
T <sub>g</sub>	Glass Transition Temperature
TE	Tissue Engineering
UC	Upconversion
UCNPs	Upconversion Nanoparticles
UV	Ultra Violet
XRD	X-Ray Diffraction

$B_2O_3$	Boron Oxide
$CaCO_3$	Calcium Carbonate
$CaO$	Calcium Oxide
$CaWO_4$	Calcium Tungstate Oxide
$Dy^{3+}$	Dysprosium ion
$Er^{3+}$	Erbium ion
$K_2O$	Potassium Oxide
$MgO$	Magnesium Oxide
$Nd^{3+}$	Neodymium ion
$Nd_2O_3$	Neodymium Oxide
$Na_2CO_3$	Sodium Carbonate
$NaPO_3$	Sodium Meta Phosphate
$P_2O_3$	Phosphorus Tri Oxide
$SiO_2$	Silicon Di Oxide
$SrAl_2O_4$	Strontium Aluminate
$Tm^{3+}$	Thulium ions
$Tm_2O_3$	Thulium Oxide
$Yb^{3+}$	Ytterbium ions
$Yb_2O_3$	Ytterbium Oxide
$YPO_4$	Yttrium Phosphate

## INTRODUCTION

The definition of tissue engineering by Langer and Vacanti is “Tissue-Engineering is an interdisciplinary biomedical field that applies principles of engineering and life sciences toward the development of biological substitutes that restore, maintain, and improve tissue function.”(Naraghi,13). Bioactive glasses (BAGs) have been largely used in tissue engineering (TE) for bone regeneration, especially silicate, borosilicate, and borate bioactive glass scaffolds with controllable degradation rate for bone tissue engineering applications (Rahaman,11). There are three types of trabecular bioactive scaffolds : Silicate (13-93), Borosilicate (13-93B1) and Borate (13-93B3). When replacing partially  $\text{SiO}_2$  by  $\text{B}_2\text{O}_3$  for example, the scaffolds can support proliferation and function of osteogenic cells (Fu,10). Borosilicate glasses are usually known for their structural stability while borate glasses have bioactive properties because of their rapid dissolution and complete conversion to HA which speed up bone healing and promote angiogenesis (Aljaman,25) (Abdelghany,13). Bioactive scaffolds are extensively used in tissue engineering for their ability to support cell growth and facilitate tissue regeneration (Stratton,16). Numerous bioactive biomaterials have been developed in the last decades, and recently different compositional modifications for further improvement of the material properties have been designed, together with different shapes, mainly three-dimensional (3D) and porous, to target the final aim (Stratton,16).

This thesis was focused on combining BAGs with luminescent crystals to develop composite multifunctional scaffolds. These scaffolds not only aim to promote healing but also target optical monitoring capabilities. An efficient technique for creating BAG scaffolds which can resemble trabecular bone and have regulated porosity is 3D printing. In 3D printing, a viscoelastic ink, constituted by BAG particulates mixed with luminescent crystals, is deposited layer by layer and sintered to create a porous structure by using the robocasting process (Magalhaes,25). We showed here that there was printability despite the presence of the luminescent crystals. The ink worked because of Pluronic was chemically interacting with the glass and getting stable.

In this thesis, rare earth (RE) doped upconverter (UC) crystals were prepared so they can release higher-energy visible light after absorbing low-energy photons, usually in the near-infrared (NIR) spectrum. Long-lasting afterglow was achieved using persistent luminescent (PeL) phosphors, such as  $\text{SrAl}_2\text{O}_4: \text{Eu}^{2+}, \text{Dy}^{3+}$ , which store energy and

release it gradually. Some applications, such as optical imaging, real-time scaffold tracking, and light-activated therapies, are made possible by including these materials in bioactive glass scaffolds (Bajestani,23).

Near-infrared (NIR) excitation is chosen for biomedical applications because of its deep tissue penetration. A functional UC phosphors are effectively excited by 980 nm lasers, but it could burn the tissue because of its intense absorption. 808 nm light is another option as it decreases water absorption and permits deeper, safer penetration, making it more suitable for *in vivo* imaging and treatment (Wang,15).

In this study, 3D-printed scaffolds were fabricated by using a borosilicate glass, combined with upconverter  $\text{Yb}^{3+}$ ,  $\text{Tm}^{3+}$ , and  $\text{Nd}^{3+}$  tri-doped  $\text{CaWO}_4$  crystals and PeL phosphor  $\text{SrAl}_2\text{O}_4: \text{Eu}^{2+}, \text{Dy}^{3+}$ . The UC crystals convert NIR light (808 nm or 980 nm) into visible emission (blue at 475 nm) which is used to charge the PeL leading to long lasting green emission. Such luminescent scaffolds have potential applications in imaging, tracking, monitoring tissue regeneration, and controlled drug delivery *in situ* (Trifanova,23). The borosilicate glass was synthesized via the melt-quench method, crushed, and milled to a fine powder suitable for 3D printing. An aqueous Pluronic F-127-based solution was added to the UC and PeL mixture together with the glass particles, and the ink was extruded into cylindrical porous scaffolds. Printed scaffolds were dried and sintered. Structural and phase analyses were obtained by using XRD, while spectroscopic characterization under UV and NIR excitation assessed the UC emission and afterglow properties. This work aims to optimize the ratio of UC crystals to PeL phosphors to achieve scaffolds with enhanced optical properties, alongside maintaining the printability of the glass matrix.

# CHAPTER 1: BACKGROUND

In this chapter, bioactive glass scaffolds, their application, and fabrication are first introduced. Then the chapter continues with luminescent materials as well as the description of the up-conversion and the PeL processes. Biophotonic Scaffolds are then introduced with their application in preventing infection, and the difference between the scaffold stimulation with either 980 or 808 nm wavelengths is explained.

## 1.1 Bioactive Glass

### 1.1.1 Bioactive Glass and Its Properties

Bioactive glasses (BAGs) are amorphous silicate-based materials that are biocompatible and capable of bonding with bone while gradually dissolving in the body (like 1393B20). These silicate-based materials allow them to stimulate new bone growth and restore damaged or diseased bone to its original structure and function (Szciodra 24 b). Figure 1 shows different glass forms, such as sintered glass bodies, sol-gel structures, and thin fibers that could be used alone and as in composite structures (Fagerlund, 12).

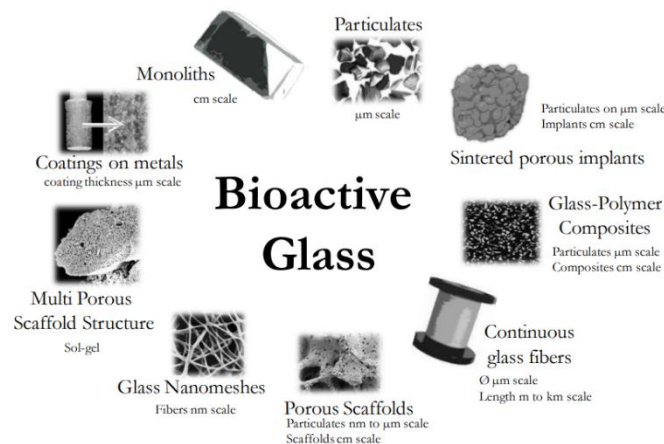


Figure 1. Different types of bioactive glass with different methods (Fagerlund,12)

In 1969, Larry Hench and his associates at the University of Florida created the first BAG, known as 45S5 Bioglass® (Hench,06). The composition of the glass was 45 SiO<sub>2</sub>, 24.5 Na<sub>2</sub>O, 24.5 CaO, and 6 P<sub>2</sub>O<sub>5</sub> (wt%). It was selected by reducing silica, increasing sodium and calcium oxides, and reducing phosphorus pentoxide. This was to have an optimal amount of ions (Na, Ca) to break the strong silica network, increasing its bioactivity (Hench,16).

The biocompatibility and chemical resemblance of HA to biological apatite found in hard human tissue are main characteristics of BAGs. As HA is osteoconductive, its precipitation on the BAGs' surfaces will promote the regeneration and integration with the existing bone and the rate at which bone apposes and integrates (Liu,25).

One of the most widely used materials for repairing bone defects is synthetic hydroxyapatite (sHA)n with the chemical formula  $\text{Ca}_{10}(\text{PO}_4)(\text{OH})_2$ . It is favored because of its close resemblance to the mineral component of natural bone, which is actually a Carbonate Hydroxyapatite. sHA is both bioactive and osteoconductive. This means it is supporting the growth of bone along its surface from the bone-implant interface, which is an ideal material for preparing a bioactive scaffold. (Jones,09).

Bioglass® was the first material shown to form a strong interfacial bond with bone tissue after implantation, with early tests in rats and monkeys showing that this bond could match or exceed the strength of native bone. Since entering clinical use in 1985, the new BAG compositions have been explored, also introducing new elements. (Jones,08)

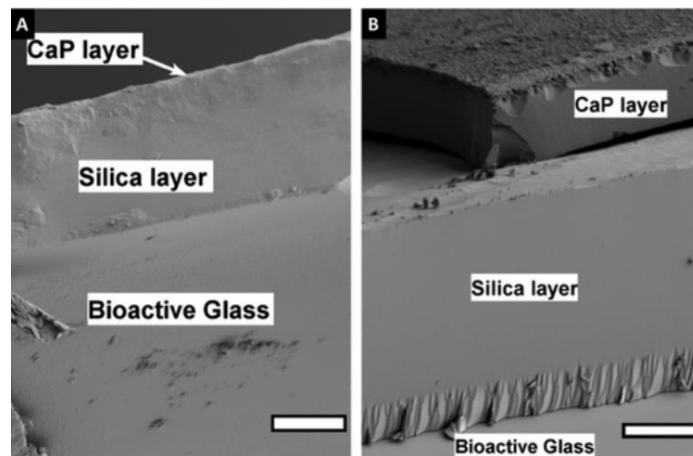


Figure 2. SEM image of cross section S53P4 (A) and 1393B20 (B) conditioned and analyzed by EDX, scale bar 20  $\mu\text{m}$  (Deraine,21)

Borosilicate glasses have recently gained significant attention due to highly encouraging results from pre-clinical studies, particularly in bone healing and regeneration. (Cannio,21). Figure 2 shows the SEM image of the cross-section of S53P4 and 1393B20. Borate and borosilicate glasses are known as promising materials due to their faster conversion kinetics into HA is faster. A study shows that boron-containing silicate glasses based on 45S5 formulation were implanted in rat bone marrow and were found to enhance bone formation. compared to pure silicate 45S5. The study of the impact of boron on the dissolution of the materials, conversion into hydroxyapatite, and the material interaction was be found in (Fabert,17).

From the material perspective, borosilicate BAGs are particularly interesting due to their lower transition temperature ( $T_g$ ) compared to silicate ones. Because of it, the sintering window is wider for the borosilicate BAGs. Therefore, these materials can be sintered more effectively than the silicate BAGs, significantly decreasing the risk of undesired crystallization phenomena, which would alter the material properties, first of all, reducing their bioactivity (Mancuso,17).

Boron ions promote osteogenesis in human adipose-derived stem cells (hADSCs), human bone marrow-derived mesenchymal stem cells (hBMSCs), murine pre-osteoblastic cells (MC3T3-E1), and myoblastic cells (C2C12) by improving the translation of mRNA encoding growth factors, which aid in angiogenesis and wound healing. Thus,  $B_2O_3$  substitution for  $SiO_2$  in 1393BAG would allow the manufacturing of porous 3D scaffolds, which support both osteogenic and angiogenic properties. Borosilicate scaffolds outperform silicate 1393BAG in bone regeneration, likely due to increased osteoclastic activity, scaffold resorption, and neovascularization mediated by 0106-B1 BAG.(Szczodra,24 b).

Moreover, borosilicate BAGs can precipitate more HA, and in a shorter time. The addition of boron to the silica network was also proven to stimulate angiogenesis, which is a fundamental feature for bone healing. (Abdelghany,13). HA supplies the oxygen, nutrients, and precursor cells needed for new bone growth. (Hankenson,11). Recent studies have shown the potential benefit of more biomimetic porous structures for bone implants, such as scaffolds. (Huang,25)

### **1.1.2. Bioactive Scaffold and Its Properties**

A bioactive scaffold is a 3D structure designed to support the regeneration of bone or other tissues by actively interacting with the surrounding biological environment. Figure 3 shows different scaffolds.

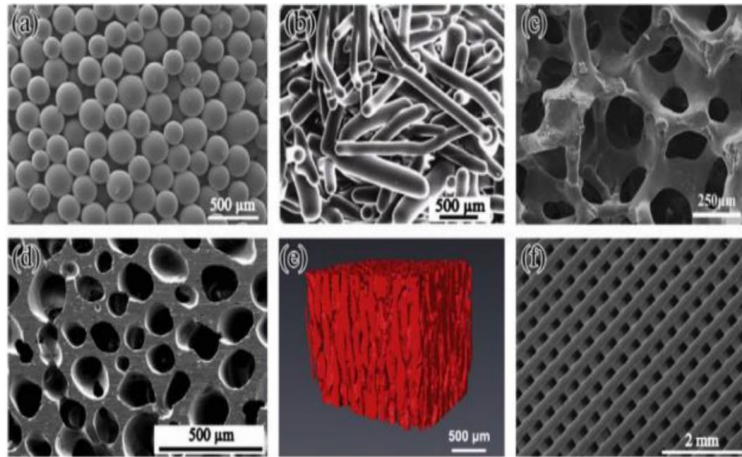


Figure 3. Microstructures of bioactive glass scaffolds made using various techniques (Rahaman,11)

Their architecture (pore size, porosity, and mechanical properties, along with surface chemistry and topography) plays a key role in cellular responses. To improve regeneration and integration, biomaterial scaffold surfaces in the tissue engineering (TE) field must have certain essential properties. The optimal 3D scaffolds should promote tissue development, migration, and cell proliferation while guaranteeing waste clearance, nutrition delivery, and oxygenation (Selim,24).

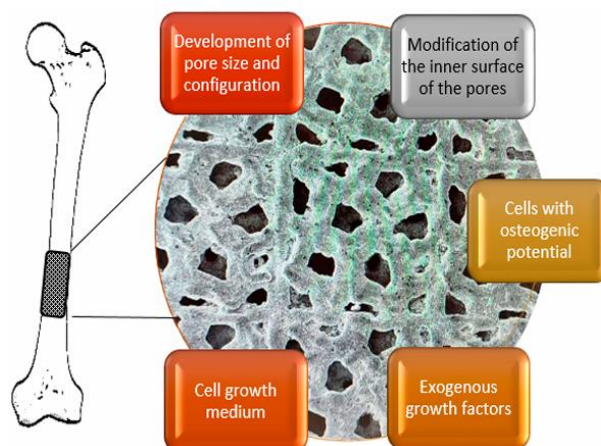


Figure 4. Algorithm for the development of an osteoconstructive porous Ti bioimplant (Kiselevskiy,23)

Bioactive scaffolds as an implant for bone should be antibacterial by adding antimicrobial compounds into the material. Its porous structures can aid in the growth of osteoblasts. Scaffolds having structures and functions comparable to real bone tissue can enhance bone cell adhesion and development, allowing bone defects to be repaired more easily (Yang,24). Figure 4 shows the algorithm for the porous Ti bioimplant.

According to bone tissue engineering, the physical and biological needs are critical for successful fabrication and implantation, as well as the growth of bone, cartilage, and

vascular tissue. Recent research has demonstrated that the combination of 3D printing technology and sophisticated biomaterials has enormous potential in bone tissue engineering. Some bioactive scaffolds are utilized for drug delivery, allowing for continuous medication release while inhibiting bacterial growth. Bioactive scaffolds can also give support and stability in bone loss throughout the mending process. (Liu 22) (Yang,24).

### 1.1.3 Fabrication of 3D Scaffold

There are usually two methods that are used for scaffold fabrication: conventional methods and advanced methods (such as 3D printing). Solvent casting, partial leaching, phase separation, gas foaming, melt molding, and freeze-drying are the most commonly utilized methods in the traditional manufacturing of scaffold techniques (Ratheesh,17). Creating 3D items is known as additive manufacturing (AM) or 3D printing. In recent years, 3D printing technology has been supporting in-plant fabrication using biomaterials. (Liu,22). The 3D printing is designed to copy cancellous bone structures, which provide a perfect environment for stem cell distribution and differentiation. Bone growth in materials with 50% interconnected porosity will reduce stress shielding effects, which is the reason material porosity becomes crucial in implant processing. It is considered a technique in biomedical engineering that demonstrates effective scaffold fabrication and cell distribution. (Ananth,24). 3D printing has properties of specific design, fabrication, low cost, and high structural complexity, which make it highly efficient in the bioengineering field (Ananth, 24). Extrusion-based printing, inkjet printing, particle fusion-based, and laser-assisted printing are now the three main categories into which the most popular 3D printing methods fall, as shown in Figure 5 (Kaur, 25).

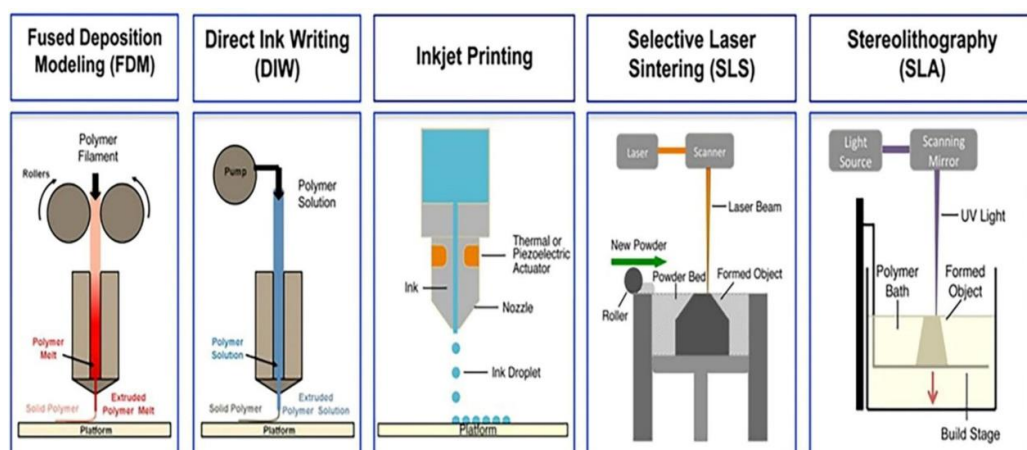


Figure 5. Schematics of different types of 3D printing (Kaur,25)

However, no single printing technology can fully capture the intricacies of different tissues; each one has its benefits and can compensate for the drawbacks and restrictions of the others (Groll, 16).

- **Extrusion-based printing:** It is one of the most common printing methods used for 3D printing of polymers and biomaterials. Fused deposition modeling (FDM) and Direct ink writing (DIW) are the two mostly used techniques of extrusion-based 3D printing (shown in Figure 5). Another name for extrusion-based printing is a nozzle-based deposition system. Fused Filament Fabrication (FFF), which is also known as FDM, is one of the most popular low-cost 3D printing methods (Azad, 20). In extrusion printing, a viscous liquid or melted filament is pushed through a nozzle and deposited layer by layer, which builds a 3D structure. FDM uses a heated nozzle to melt and extrude thermoplastic filaments like polylactic acid (PLA), while DIW operates at lower temperatures by using hydrogels or polymer solutions that solidify through cooling, cross-linking, or thixotropic behavior. The method is especially suited for tissue engineering applications where scaffolds and biomedical structures are required, as it allows good control over geometry and porosity. Despite of many advantages, extrusion-based printing often faces limitations related to weak stability, slow printing speed, and reduced resolution compared to optical-based systems (Kaur,25) (Ananth,24).
- **Inkjet printing:** There are two types of inkjet systems usually used, which are continuous inkjet (CIJ) and drop-on-demand (DOD). In recent years, inkjet printing has gained widespread attention in the research fields of polymer molding, nanocomposites, and tissue engineering. But low cell density affects this printing process, and the range of viscosities of the associated printing materials used is rather constrained. The advantages of inkjet printing are its high printing resolution, low technical cost, and the ability to print numerous materials at once. (Li,20) (Saunders,14) (Kaur,25)
- **Particle fusion-based printing:** This 3D printing technique uses the powder particles that are fused or bonded together layer by layer to create a 3D structure. The two main categories of particle fusion-based printing are selective laser sintering (SLS) and particle binding (PB). Figure 5 illustrates the schematic picture of SLS. In SLS, a laser beam scans and fuses fine metal, polymer, or ceramic powders by heating them slightly above their melting point. On the other hand, P uses a liquid binder to adhere particles in each layer, which are later solidified through heat treatment or sintering. Both techniques are widely used in industrial prototyping and the production of complex geometries in materials. Due to their high mechanical strength and fine resolution, these techniques are particularly valuable in the fabrication of orthopedic implants, dental devices, aerospace components, and bioceramic scaffolds. Although particle-fused

printing tends to be expensive and time-consuming because of the high energy requirements and complex equipment setup (Kaur,25) (Ananth,24).

- **Light-assisted printing:** Light-assisted printing are usually three types, such as, Stereolithography (SLA), Digital Light Processing (DLP), and Two-Photon Lithography (2PL). It is also known as photopolymerization-based printing. This method involves UV or visible light that cures photosensitive resins into solid structures. These methods are popular for biomedical applications like microfluidic devices and dental implants. (Kaur,25) (Ananth,24).

## 1.2 Luminescent Materials

### 1.2.1 Rare Earth ions

Rare-earth (RE) elements in the periodic table constitute the 15 elements also known as "lanthanides" and have atomic numbers ranging from 57 (lanthanum) to 71 (lutetium) (Figure 6). RE elements, particularly the trivalent lanthanide ions ( $\text{Ln}^{3+}$ ), play a crucial role in the field of luminescent materials due to their unique electronic configurations, such as  $4f-4f$  and  $4f-5d$  electronic transitions, and possess sharp emission spectra. The most commonly used luminescent rare earth ions include  $\text{Eu}^{3+}$ ,  $\text{Tb}^{3+}$ ,  $\text{Sm}^{3+}$ ,  $\text{Dy}^{3+}$ ,  $\text{Ce}^{3+}$ ,  $\text{Nd}^{3+}$ ,  $\text{Er}^{3+}$ ,  $\text{Tm}^{3+}$ , and  $\text{Yb}^{3+}$ , each of which exhibits characteristic emission wavelengths. Few lanthanide ions show luminescence in the visible or NIR regions with UV (ultraviolet) radiation. The color of the emitted light depends on these ions; for example,  $\text{Eu}^{3+}$  emits red light,  $\text{Tb}^{3+}$  green light,  $\text{Sm}^{3+}$  orange light, and  $\text{Tm}^{3+}$  blue light.  $\text{Yb}^{3+}$ ,  $\text{Nd}^{3+}$  and  $\text{Er}^{3+}$  are well-known for their near-infrared luminescence (Binnemans,09).

**Periodic Table of the Elements**

ELEMENT GROUPS																																																																																																	
Non Metals	Alkali Metals	Halogens	Alkali Earth Metals	Noble Gases	Transition Metals	Metals	Lanthanides	Metalloids	Actinides																																																																																								
1	2																	10	11																																																																														
H	He																	Ne	Ar																																																																														
3	4																	12	13	14	15	16	17	18																																																																									
Li	Be																	B	C	N	O	F	Ne																																																																										
5	6																	13	14	15	16	17	18																																																																										
Na	Mg																	Al	Si	P	S	Cl	Ar																																																																										
7	8	9	10	11	12	13	14	15	16	17	18	19	20	21	22	23	24	25	26	27	28	29	30	31	32	33	34	35	36																																																																				
K	Ca	Sc	Ti	V	Cr	Mn	Fe	Co	Ni	Cu	Zn	Ga	Ge	As	Se	Br	Kr																																																																																
17	18	19	20	21	22	23	24	25	26	27	28	29	30	31	32	33	34	35	36																																																																														
Rb	Sr	Y	Zr	Nb	Mo	Tc	Ru	Rh	Pd	Ag	Cd	In	Sn	Sb	Te	I	Xe																																																																																
21	22	23	24	25	26	27	28	29	30	31	32	33	34	35	36	37	38	39	40	41	42	43	44	45	46	47	48	49	50	51	52	53	54	55	56	57	58	59	60	61	62	63	64	65	66	67	68	69	70	71	72	73	74	75	76	77	78	79	80	81	82	83	84	85	86	87	88	89	90	91	92	93	94	95	96	97	98	99	100	101	102	103	104	105	106	107	108	109	110	111	112	113	114	115	116	117	118
Cs	Ba	La	Hf	Ta	W	Re	Os	Ir	Pt	Au	Hg	Tl	Pb	Bi	Po	At	Rn																																																																																
37	38	39	40	41	42	43	44	45	46	47	48	49	50	51	52	53	54	55	56	57	58	59	60	61	62	63	64	65	66	67	68	69	70	71	72	73	74	75	76	77	78	79	80	81	82	83	84	85	86	87	88	89	90	91	92	93	94	95	96	97	98	99	100	101	102	103	104	105	106	107	108	109	110	111	112	113	114	115	116	117	118																
Fr	Ra	Ac	Rf	Db	Sg	Bh	Hs	Mt	Ds	Rg	Cn	Nh	Fl	Mc	Lv	Ts	Og																																																																																
		Lanthanides																																																																																															
		La	Ce	Pr	Nd	Pm	Sm	Eu	Gd	Tb	Dy	Ho	Er	Tm	Yb	Lu																																																																																	
		Actinides																																																																																															
		Ac	Th	Pa	U	Np	Pu	Am	Cm	Bk	Cf	Es	Fm	Md	No	Lr																																																																																	

Figure 6. Period table of the rare earth elements (E-tech resources,21)

In terms of average crustal abundance, rare earth (RE) elements are quite uncommon. The quantity of concentrated RE element deposits is restricted. The RE elements have

a wide range of military, industrial, energy, and defense technology uses due to their unique physical and chemical characteristics (Walters,11).

Since the majority were classified as "Rare earth" in the 18th and 19th centuries. The most prevalent RE elements are Cerium, which is actually more prevalent in the crust of the Earth than lead or copper. In the Earth's crust, all of the RE elements—aside from promethium—are generally more prevalent than silver, gold, or platinum. In terms of average crustal abundance, RE elements are concentrated and economical rather than scarce. Because of their special magnetic, luminous, and catalytic qualities, these elements are essential to many contemporary technologies (Balaram,19).

The elements lanthanum, cerium, neodymium, and yttrium are examples of common rare earth elements. They are necessary for the synthesis of phosphors for display screens (europium and yttrium), catalysts in the refinement of petroleum (cerium), and high-strength magnets (neodymium and dysprosium). Here, the separation of RE extract oxides from solvent extraction is shown in Figure 7.

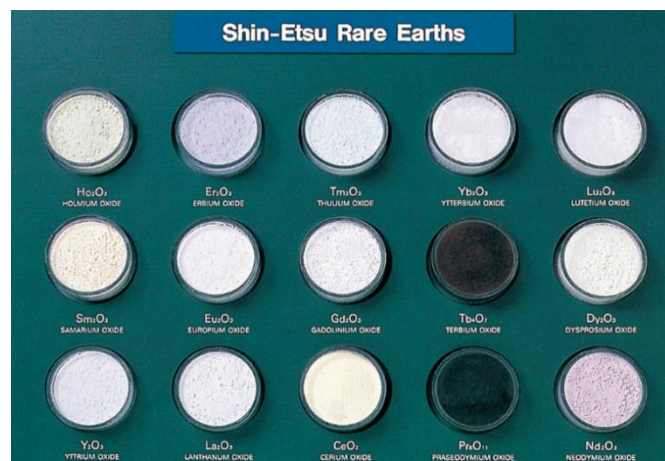


Figure 7. Separated RE extract oxides from solvent extraction (Shin-Etsu RE)

Energy-efficient lights, electric cars, wind turbines, and other green technologies all depend on RE elements. The glass industry is the leading consumer of RE elements. Example: Europium is the common dopant for the optical fibers. Also, Synthetic jewels, laser crystals, microwave devices, superconductors, sensors, nuclear control rods, and cryo-coolers are other products that use rare-earth elements. The usage of RE elements as nano-filters and in memory devices, power converters, optical clocks, infrared decoy flares, and fusion energy are important new applications. The applications of RE elements in the technology field are increasing gradually. (Gosen,17)

### 1.2.2. Upconversion Process

Luminescence is the emission of light by a substance that has absorbed energy, without the involvement of high temperature. In luminescence, the absorbed energy excites electrons to higher energy levels, and when these electrons return to their lower or ground states, they release the excess energy in the form of visible, ultraviolet, or infrared light .. The word 'Luminescence' was coined by German Physicist Eilhard Weidemann in 1888. This phenomenon is important to the development of solid-state white light-emitting diodes (LEDs). Which are quickly replacing traditional lighting technologies Luminescent materials, especially those activated by rare earth (RE<sup>3+</sup>) ions, are identified by their stability, long-lasting glow, considerable variations in light emission wavelength, and accurate emission lines. (Sharma,18) These features have led to its application in a wide range of sectors, including laser technology, materials science, agriculture, medical diagnostics, and others. Applications span from lighting, displays, lasers, and radiation detection systems to optical telecommunications, security inks, and bioconjugates for photodynamic treatment of cancer. Figure 8 shows the properties and characteristics of the RE elements.

Atomic number	n*	Element	Electron configuration RE <sup>3+</sup>	Ground term RE <sup>3+</sup>
58	1	Cerium - Ce	4f <sup>1</sup> 5s <sup>2</sup> 5p <sup>6</sup>	<sup>2</sup> F <sub>5/2</sub>
59	2	Praseodymium - Pr	4f <sup>2</sup> 5s <sup>2</sup> 5p <sup>6</sup>	<sup>3</sup> H <sub>4</sub>
60	3	Neodymium - Nd	4f <sup>3</sup> 5s <sup>2</sup> 5p <sup>6</sup>	<sup>4</sup> I <sub>9/2</sub>
61	4	Promethium - Pm	4f <sup>4</sup> 5s <sup>2</sup> 5p <sup>6</sup>	<sup>5</sup> I <sub>4</sub>
62	5	Samarium - Sm	4f <sup>6</sup> 5s <sup>2</sup> 5p <sup>6</sup>	<sup>6</sup> H <sub>5/2</sub>
63	6	Europium - Eu	4f <sup>7</sup> 5s <sup>2</sup> 5p <sup>6</sup>	<sup>7</sup> F <sub>0</sub>
64	7	Gadolinium - Gd	4f <sup>7</sup> 5s <sup>2</sup> 5p <sup>6</sup>	<sup>8</sup> S <sub>7/2</sub>
65	8	Terbium - Tb	4f <sup>9</sup> 5s <sup>2</sup> 5p <sup>6</sup>	<sup>7</sup> F <sub>6</sub>
66	9	Dysprosium - Dy	4f <sup>9</sup> 5s <sup>2</sup> 5p <sup>6</sup>	<sup>6</sup> H <sub>15/2</sub>
67	10	Holmium - Ho	4f <sup>10</sup> 5s <sup>2</sup> 5p <sup>6</sup>	<sup>5</sup> I <sub>8</sub>
68	11	Erbium - Er	4f <sup>11</sup> 5s <sup>2</sup> 5p <sup>6</sup>	<sup>4</sup> I <sub>15/2</sub>
69	12	Thulium - Tm	4f <sup>12</sup> 5s <sup>2</sup> 5p <sup>6</sup>	<sup>3</sup> H <sub>6</sub>
70	13	Ytterbium - Yb	4f <sup>13</sup> 5s <sup>2</sup> 5p <sup>6</sup>	<sup>2</sup> F <sub>7/2</sub>

\*Number of electros (n) in the 4f shell of three-valence Rare Earth ions.

*Figure 8. Properties and Characteristics of the RE elements (Prajzler, 10)*

The upconversion (UC) mechanism is a process where two or more low-energy photons (e.g., Infrared) are absorbed and their energy is combined to emit a single higher-energy

photon (e.g., visible or ultraviolet). There are different energy transfer processes during UC events, and these are: Energy transfer upconversion (ETU), Excited-state absorption (ESA), Photon avalanche (PA), Cooperative UC (CUC), and Energy migration-mediated UC (EMU). The energy level diagrams of these processes are shown in Figure 9 (Thirumalai,16).

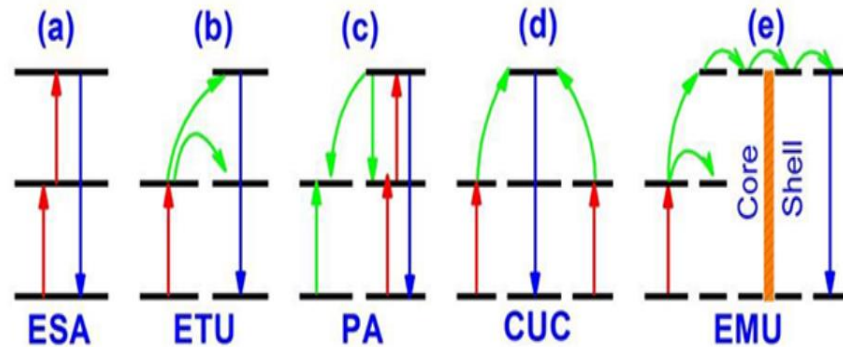


Figure 9. Simplified energy level diagrams describing up-conversion processes: (a) ESA, (b) ETU, (c) PA, (d) CUC, and (e) EMU (red: excitation; blue: UC emission, green: energy transfer)(Thirumalai,16)

- ESA: In ESA, a single ion absorbs two or more low-energy photons one after another. This moves the ion from the ground state to an excited state, leading to upconversion emission as shown in Figure 9 a. It works best at low doping levels because high concentrations can lead to energy loss. But ESA is not very efficient because of the weak absorption. The weak absorption happens due to the forbidden transition of the rare-earth ions.
- ETU: There are two types of ions: a sensitizer and an activator. The sensitizer absorbs energy and passes it to the activator, which emits light. ETU is more efficient than ESA because energy transfer between ions is smoother and long-lasting. It requires the two ions to be closer together and have matching energy levels.
- PA is a more complex process that needs high light intensity to start. It begins with regular absorption, followed by more energy being added through ESA or ETU. It creates a feedback loop that makes it very efficient, but only under strong pumping conditions.
- CUC also uses sensitizer and activator ions, like ETU, but it works differently but less efficient. This is common in  $\text{Yb}^{3+}/\text{RE}^{3+}$  systems. Here, two sensitizers transfer energy at the same time to one activator.

- EMU: The EMU process involves four types of luminescent centers: sensitizer, accumulator, migrator, and activator. The sensitizer/accumulator and the activator are confined in separate layers of the core shell. An activator within the shell traps the migrating energy, causing it to emit UC light (Thirumalai,16).

This study aims to achieve blue upconversion with an  $\text{Nd}^{3+}$  doped crystal under 808nm excitation. Basically, among all the  $\text{RE}^{3+}$  ions,  $\text{Nd}^{3+}$  ions have a large absorption cross-section at 808nm. In contrast,  $\text{Yb}^{3+}$  plays a role as an important energy transfer bridge between  $\text{Nd}^{3+}$  and other  $\text{RE}^{3+}$  (like Er, Ho, Tm) ions, when  $\text{Nd}^{3+}/\text{Yb}^{3+}/\text{RE}^{3+}$  triply doped samples are excited by 808 nm. The  $\text{Yb}^{3+}$  ion has no matched energy levels near this wavelength to absorb. Upon 980 nm excitation,  $\text{Nd}^{3+}/\text{Yb}^{3+}/\text{RE}^{3+}$  triple-doped phosphors can also produce effective UC emission of  $\text{RE}^{3+}$ . As stated earlier, the  $\text{Tm}^{3+}$  ion is a blue UC activator, which emits blue emission when  $\text{Tm}^{3+}$  doped materials are excited by infrared light. Recently,  $\text{Nd}^{3+}/\text{Yb}^{3+}/\text{Tm}^{3+}$  triply doped fluorescence materials have drawn attention for their efficient blue emission under the excitation of 800 nm, and the underlying energy transfer mechanism (Tian,20) (Soderlund,15).

Here,  $\text{CaWO}_4$  (Calcium tungstate) was chosen as a host material as it is one of the most promising materials for upconversion applications. When it is co-doped with  $\text{Yb}^{3+}/\text{Tm}^{3+}$ , it emits blue emission under 980nm excitation. Also, some advantages have been shown for using  $\text{CaWO}_4$  crystals as a blue upconverter, facile fabrication conditions via solid-state synthesis, and high activator concentrations.  $\text{CaWO}_4$  also exhibits good thermal stability. (Magalhaes,25). In this experiment,  $\text{CaWO}_4: \text{Yb}^{3+}/\text{Tm}^{3+}/\text{Nd}^{3+}$  was used as the doped ion. The crystals were examined under 808 nm and 980 nm excitation.

### 1.2.3 Persistent Luminescence (PeL) Process

PeL is a type of luminescence in which a material continues to emit light for a longer duration even after the excitation source (such as UV or visible light) is turned off. Persistent Luminescence has a long history, over a thousand years. By the early 17th century, persistent luminescence gained significant attention after the discovery of the famous Bologna Stone. The persistent luminescence originates from the monovalent copper impurity. The first commercial persistent phosphors, like  $\text{ZnS: Cu}$ , appeared about 100 years ago for self-lit watch dials. But the breakthrough came in the mid-1990s with efficient  $\text{Eu}^{2+}$ ,  $\text{RE}^{3+}$  co-doped aluminated  $\text{CaAl}_2\text{O}_4: \text{Eu}^{2+}$ ,  $\text{Nd}^{3+}$ , and  $\text{SrAl}_2\text{O}_4: \text{Eu}^{2+}$ ,  $\text{Dy}^{3+}$  emitting in the blue and green, which offer long afterglow and solar charging capability. Among those,  $\text{Y}_2\text{O}_2\text{S: Eu}^{3+}$ ,  $\text{Mg}^{2+}$ , Ti achieved commercial success because of their red emission (Brito,12). Nowadays, it is possible to have persistent luminescence phosphors to cover the entire visible spectral range (Figure 10)



Figure 10. Three-color persistent luminescence panel based on the  $\text{Sr}_2\text{MgSi}_2\text{O}_7:\text{Eu}^{2+}, \text{Dy}^{3+}$  (blue),  $\text{SrAl}_2\text{O}_4:\text{Eu}^{2+}, \text{Dy}^{3+}$  (green), and  $\text{Y}_2\text{O}_2\text{S}:\text{Eu}^{3+}, \text{Mg}^{2+}, \text{Ti}$  (red) phosphors (Brito,12)

The PeL mechanisms were largely speculative. It cannot provide a quantitative understanding of materials and processes; for example, the mechanism of PeL in  $\text{Eu}^{2+}$  and  $\text{R}^{3+}$  doped  $\text{SrAl}_2\text{O}_4$ , considered as one of the fundamental ones, is purely qualitative and contains highly suspicious processes as charge transfer emission of  $\text{Eu}^{2+}$  at 445 nm. But it is possible to predict the mechanism by understanding the following: the nature of an electron and hole transfer, the charging process of the persistent luminescence, Identify the most probable centers for it. The role of RE co-dopants, and 4. to predict the energy sufficient to charge persistent luminescence (Brito,12).

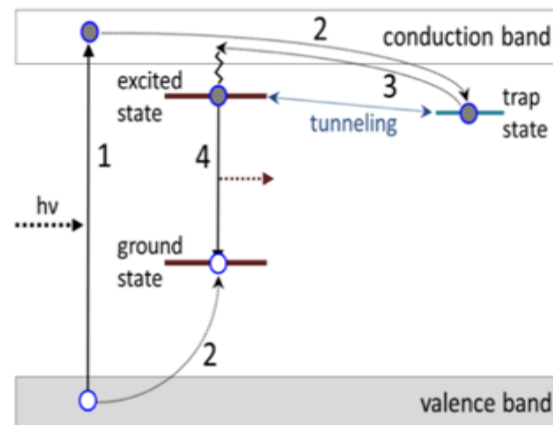


Figure 11. Schematic diagram of a persistent luminescence mechanism under band-to-band (Xu,19)

The PeL process begins with the excitation phase (according to Figure 11), during which electrons are stimulated and holes are formed under the light. These excited electrons are subsequently trapped non-radiatively by electron (or hole) traps using methods involving the conduction (valence) band or quantum tunneling, a process known as trapping. Following this, de-trapping happens when electrons are liberated as a result of thermal stimulation. Finally, the liberated electrons return to the emission center and recombine with holes, resulting in delayed luminescence. (Xu,19)

The  $\text{SrAl}_2\text{O}_4: \text{Eu}^{2+}, \text{Dy}^{3+}$  phosphor is well-known for its green emission and long decay time (Francisco,21). According to some studies,  $\text{SrAl}_2\text{O}_4: \text{Eu}^{2+}, \text{Dy}^{3+}$  PeL phosphors with  $\text{Yb}^{3+}, \text{Tm}^{3+}$  co-doped crystals can show a green afterglow under UV and 980nm excitation. This happened because the upconversion process of  $\text{Yb}^{3+}$  and  $\text{Tm}^{3+}$  leads to and blue light which is used to charge the phosphors (Magalhaes,23). Here,  $\text{SrAl}_2\text{O}_4: \text{Eu}^{2+}, \text{Dy}^{3+}$  used as a PeL phosphor with the tri-doped  $\text{CaWO}_4: \text{Yb}^{3+}, \text{Tm}^{3+}, \text{Nd}^{3+}$  crystal.

## 1.3 Applications of 3D Printed Scaffold

### 1.3.1 Green Light Use of Prevent Infection

The (NIR) afterglow of persistent luminescence nanoparticles has attracted a lot of attention as a highly sensitive luminescent probe for optical imaging. Modern public health advocates for three stages of prevention: prognosis, treatment, and prevention. These days, antimicrobial methods based on nanotechnology, such as photodynamic therapy (PDT), chemodynamic therapy (CDT), sonodynamic therapy (SDT), and photothermal therapy (PTT), are used to treat infections (Wang,23).

To detect and control possible public health risks in their early phases, the primary prevention stage is generally acknowledged as the most crucial stage, which requires the use of quick and accurate screening instruments (Wang,23)

$\text{SrAl}_2\text{O}_4: \text{Eu}^{2+}, \text{Dy}^{3+}$  is a desirable inorganic photo luminescence material (PLM) with green emission characteristics and long-lasting afterglow time. This phosphor is conceivably promising as an internal rechargeable light source for persistent PDT. More importantly, the presence and release of  $\text{Sr}^{2+}$  ion achieve potent osteointegration and improve the osteogenic bioactive properties. Green light can stress bacterial membranes by exciting endogenous or material-based photosensitizers, which produce relative oxygen, causing oxidative and structural damage to the bacterial cell envelope (Huang,24).

### 1.3.2 Excitation Using 808 nm and 980 nm

In this section, the definition, efficiency of 808 nm and 980 nm excitation are discussed. Their comparison and laser effect on the human body are also stated.

**808 nm laser** : falls within the infrared spectrum. It is not visible to the human eye but can be detected using specialized sensors. Less absorbable by water can make it useful for medical and imaging applications. Often used to excite lanthanide-doped upconversion nanoparticles (UCNP).

**980 nm laser** : falls in the NIR region of the EM (electromagnetic) spectrum. It is also not visible like 808nm. It is useful for medical treatments, fiber optic communication, and excites UCNPs.

**980 nm vs. 808 nm** : Some materials exhibit better absorption at 808 nm compared to 980 nm. If the sample has higher absorption efficiency at 808 nm, it can get stronger luminescence signals, which makes it easier to detect and measure accurately. In some cases, an 808 nm laser can help to reduce background interference or noise in the luminescence spectrum. This is important for achieving more accurate measurements. The choice of laser wavelength can also depend on the sensitivity and spectral range of the detection equipment. A study shows that 808 nm of light penetrates as much as 54% deeper than 980 nm of light in bovine tissue. Power measurements were taken for each wavelength at the various depths. (Hudson,13). In Figure 12 demonstrates the laser light pattern at 808nm and 980nm at the tissue sample.

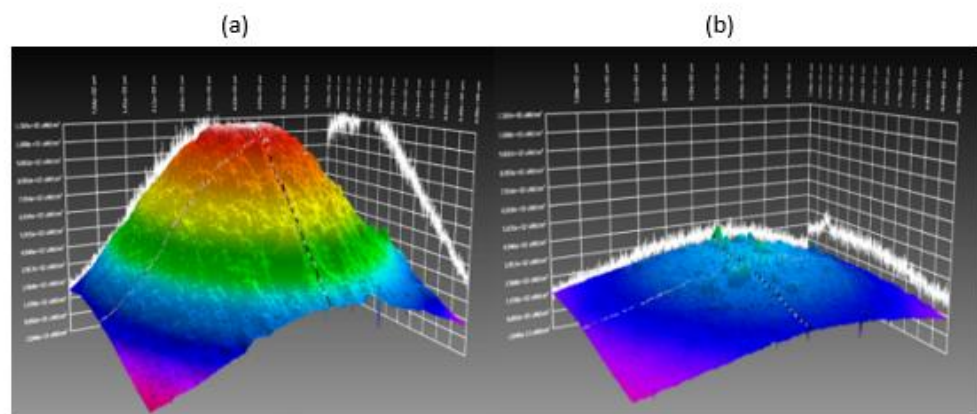


*Figure 12. (a) Laser light pattern 808 nm at 3.3 cm tissue depth, (b) Laser light pattern 980 nm at 2.8 cm tissue depth (Hudson,13)*

One of the most important issues that needs to be considered while using lasers is safety. In PDT, to assess the danger of NIR laser-induced tissue burning, the real-time temperature of a mouse's skin was measured with a laser power density of  $1.5 \text{ Wcm}^{-2}$  for 15 minutes. Before irradiation, carcinoma cell line (CAL 27) tumor cells were injected into the mouse's right and left thighs to emphasize the irradiation region. After 15 minutes of irradiation with a 980 nm laser, the tumor tissue temperature increased, and the edema site became encrusted due to thermal injury. But the 808 nm laser caused no harm. (Chan,17) Despite some comparisons, 808 nm and 980 nm work together became a good example of the wavelength coupling technology. To improve the metal processing, like metal cladding or welding, several diode laser beams were used to be together and worked as a single beam. By this, the efficiency of the beam becomes more than 60%. This is good enough for practical use in metal processing (Gu,12).

## CHAPTER 2: EXPERIMENTAL PART

### 2.1 Bioactive Scaffold Preparation

In this study, bioactive scaffolds were 3D printed using a 3D printer. The scaffolds consist of bioactive glass as in (Szczodra, 24 a), blue upconverter crystal  $\text{CaWO}_4: \text{Yb}^{3+}, \text{Tm}^{3+}, \text{Nd}^{3+}$  and green PeL phosphors.

#### 2.1.1 Glass Melting

The bioactive glass used for this study is 1393B20, which is an experimental borosilicate glass composition. The nominal composition is shown in Table 1. For the experiment, the glass was prepared from analytical grade precursors  $\text{Na}_2\text{CO}_3$  (Thermal Scientific, 99.95%),  $\text{NH}_4\text{H}_2\text{PO}_4$  (Sigma-Aldrich, 98%),  $\text{CaCO}_3$  (Alfa Aesar, 99.5%),  $\text{MgO}$  (Aldrich, 99%),  $\text{H}_3\text{BO}_3$  (Sigma, 99.5%),  $\text{K}_2\text{CO}_3$  (Sigma, 99%), and Belgian quartz sand. 1393B20 glasses were melted in 60g (gram) batches using platinum crucibles. Precisely, the precursors were heated up at  $800\text{ }^\circ\text{C}$  with a rate of  $16\text{ }^\circ\text{C}/\text{min}$  in air inside LHT 02/17 LB speed electric furnace (Nabertherm GmbH, Lilienthal, Germany), kept at this temperature for 15 minutes, and successively heated up to  $1450\text{ }^\circ\text{C}$  with a rate of  $13\text{ }^\circ\text{C}/\text{min}$ . The melt was finally kept at  $1450\text{ }^\circ\text{C}$  for 30 minutes.

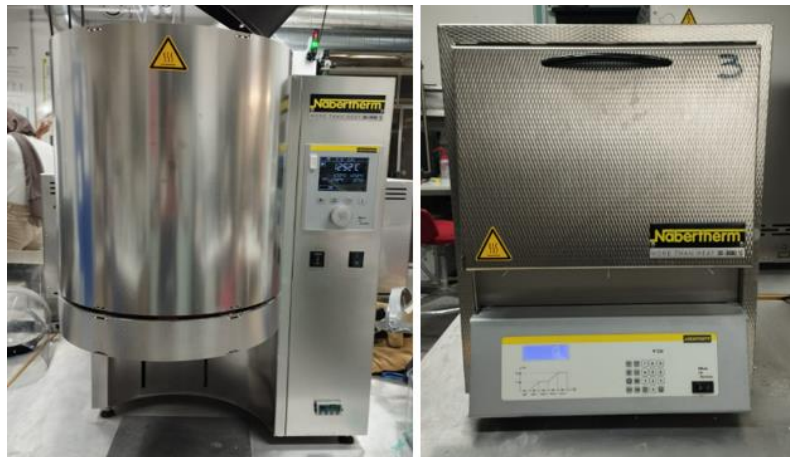


*Figure 13. Picture of furnaces used for glass melting and annealing*

The melt was cast in a graphite mold and annealed in an electric muffle furnace (Nabertherm L3/2) for 8 hours at  $500\text{ }^\circ\text{C}$  to release the glass tension. The glass was then crushed first by using a mortar and pestle, then by ball-milling, to get the final particle size  $< 38\text{ }\mu\text{m}$  (micrometer). The obtained glass powders were stored in a desiccator and used within 2 months. Figure 13 illustrates the furnaces used for glass melting and annealing.

**Table 1 Nominal Glass Composition (mol%)**

Glass	SiO <sub>2</sub>	B <sub>2</sub> O <sub>3</sub>	P <sub>2</sub> O <sub>5</sub>	Na <sub>2</sub> O	K <sub>2</sub> O	CaO	MgO
1393B20	43.68	10.9	1.7	6	7.9	22.1	7.7

### 2.1.2 Crystal Synthesis

CaWO<sub>4</sub>: Yb<sup>3+</sup>, Tm<sup>3+</sup> [Ca<sub>1-2(x+y)</sub> WO<sub>4</sub>Yb<sub>x</sub>Tm<sub>y</sub>Na<sub>(x+y)</sub>] crystals with y=0.25 at% and x= 2.5, 5, 7.5, 10 and 12.5 at% were prepared by using solid state reaction. The starting raw materials were CaCO<sub>3</sub> (Alfa-Aesar technical grade), WO<sub>3</sub> (honey-well-Fluka,99%), Yb<sub>2</sub>O<sub>3</sub> (Sigma-Aldrich,99.9%), Tm<sub>2</sub>O<sub>3</sub> (Honeywell ≥ 99%), and Na<sub>2</sub>CO<sub>3</sub> (Sigma-Aldrich 99.9%). Crystals are labelled as Yb<sub>x</sub>Tm<sub>0.25</sub> (y=0.25 at%). After the characterization, four more crystals with the Yb<sup>3+</sup> (7.5 and 10 at.%) content with different amounts of Tm<sup>3+</sup> (0.125 and 0.5 at%).were prepared. Then, CaWO<sub>4</sub>: Nd<sup>3+</sup>, Tm<sup>3+</sup> crystals prepared with 0.5at% Tm<sub>2</sub>O<sub>3</sub> and Nd<sub>2</sub>O<sub>3</sub> 5, 10 &15 at%. The raw chemical used for Nd<sup>3+</sup> was Nd<sub>2</sub>O<sub>3</sub> (Sigma-Aldrich, 99.99%). For the final tri-doped crystal, CaWO<sub>4</sub>: Yb<sup>3+</sup>,Tm<sup>3+</sup>,Nd<sup>3+</sup>[Ca<sub>1-2(x+y)-z</sub>WO<sub>4</sub>Yb<sub>x</sub>Tm<sub>y</sub>Nd<sub>z</sub>Na<sub>(x+y)</sub>] where the doping concentrations of Yb<sup>3+</sup> and Tm<sup>3+</sup> were respectively 10at% and 0.25at%, and the concentration of Nd<sup>3+</sup> varied from 0.125,0.25,0.5,1,2,3 and 5 at%.

For the crystal preparation, the batches were prepared by individual weighing of chemicals according to the batch calculation. They were placed in a mortar, blended, and placed in an Alumina crucible. The chemicals were mixed and heated at 1200°C using a 3°C per minute heating rate in an ambient atmosphere. The duration of the thermal treatment was 4 hours. After that, the crystal well crushed in a mortar again, and the process was repeated with the same heat treatment.

### 2.1.3 3D Printing

Ink was prepared using Pluronic ® F-127 (Sigma-Aldrich, USA) as a binder for the solid particles and sacrificial template supporting the printing process. Pluronic ® F-127 aqueous solution was prepared with a concentration of 30 wt%, by mixing in a plastic jar 15g Pluronic ® F-127 powder and 35g distilled water. The jar was then sealed and placed into an ice bath, and the solution was mixed with a magnetic stirrer at high RPM for at least 6 hours, to guarantee its homogeneity. The whole process was done in the ice bath to maintain the viscosity of the Pluronic ® solution low enough to be effectively stirred. This, because at higher temperatures, it starts to reversibly gelify, while at lower temperatures (around 4°C) it is liquid (Chavez,06). After the mixing, the solution was

kept in the fridge and used within 12 months. Prepared aqueous Pluronic solution are shown in Figure 14.

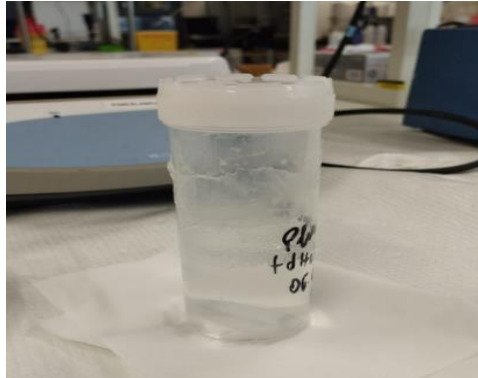


*Figure 14. As-prepared Pluronic® F-127 aqueous solution.*

For the ink, we used 85 wt% 1393B20 glass, 5 and 7.5 wt% UC crystals ( $\text{CaWO}_4$ :  $\text{Yb}^{3+}/\text{Tm}^{3+}/\text{Nd}^{3+}$ ), 10 and 7.5 wt% PeL phosphors, and 30 wt% Pluronic. This UC-PeL ratio was found to be the most promising ratio for efficient charging of the PeL phosphors by the blue UC crystals using 980 nm (results as shown in Figure 29).

When the Pluronic solution is ready, the ink preparation starts with mixing the components. Here, we prepare two compositions and one glass sample for 3D printing. The composition of the UC, PeL, and glass is given in the table below.

**Table 2. Composition of UC-PeL Glass Powder**

Pluronic	UC Crystal	PeL	Glass
(a) 2.8g (30 wt%)	–	–	3.12g (100 wt%)
(b) 2.8g (30 wt%)	0.156g (5 wt%UC)	0.312g (10 wt%PeL)	2.652g (85 wt%)
(c) 2.8g (30 wt%)	0.234g (7.5 wt%UC)	0.234g (7.5 wt%PeL)	2.652g (85 wt%)

2.8 g Pluronic (30 wt%) solution, added with all the components to prepare the ink for 3D printing, was measured on the scale. Then, the ink was vortexed for 5 cycles, alternating 30 seconds of vortexing and 30 seconds of cooling in the ice bath, in order to make it homogeneous. After that, the ink was injected with a 10 ml syringe and transferred to the 3D printing cartridge. The ink was left to set for 1 hour at room temperature before printing, after covering the cartridge with parafilm. The 3D printing must be done within

a few hours after the ink preparation, because the ink tends to dry and solidify at room temperature, probably because of the effect of the gelification of Pluronic® solution. During the whole procedure, the formation of bubbles in the ink should be avoided to guarantee good printability. The syringe was placed and attached to the 3D printer (3Dn Tabletop Printer, nScript Inc., Orlando, Florida, USA). Figure 15 shows the 3D printing process with 5 wt% UC-10wt%PeL mix. The printing parameters were set using Machine Tool 3.0 software. The pressure was set between 20 and 30 psi for the inks containing UC/PeL, while between 15 and 25 psi for the control ink (1393B20).

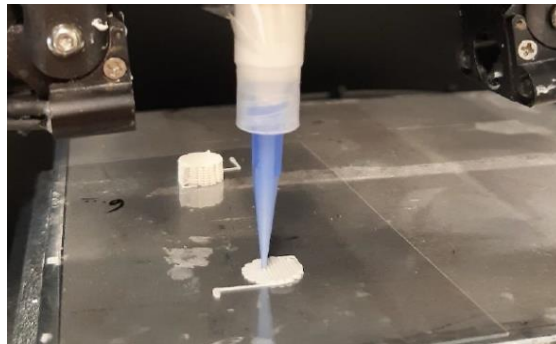


*Figure 15. Image of the 3D printing process with 5 wt% UC-10 wt% PeL mix.*

We prepared cylindrical porous scaffolds (diameter~6mm × height~2.5 mm) from the three different ink compositions. Every scaffold takes 2 to 3 minutes to be printed. The ink showed green PeL in the dark shown in Figure 16.

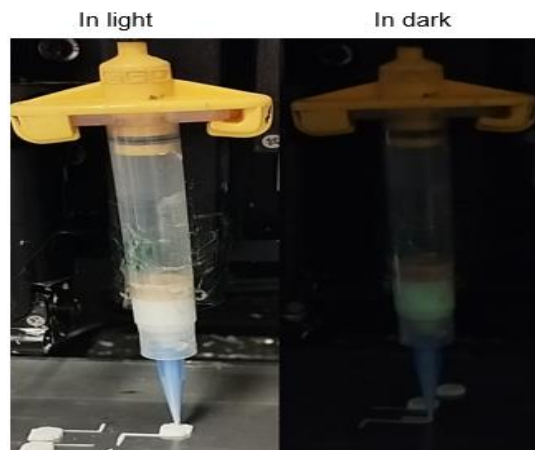


*Figure 16. Visible green PeL in the ink.*

Afterward, the printing scaffolds were left to dry at 37 °C for at least 24 hours. The 3D printed Scaffolds are very fragile. So it always needs to be handled carefully. The samples were successively sintered. For sintering, the samples are placed in the oven heated up to 625 °C at a rate of 10.5 °C/min, and kept at this temperature for 1 hour. After that, the sintered scaffolds are extracted from the oven when the temperature was

below 40 °C, to prevent any thermal shocks, possibly causing cracks or fractures in the scaffolds. Half of the scaffolds were left unsintered as a control.

## 2.2.XRD Analysis

XRD is a non-destructive method for determining a material's composition and structure. There are two basic methods for producing X-rays. One is associated with electric transitions between atoms' K-shells, while the other is related to electrons decelerating in an electric field, which produces a wide range of X-rays (Cullity,78).

The latter produces narrow, sharp spectral peaks whose wavelength changes depending on the electrical structure of the substance. X-rays are created in an X-ray tube by bombarding a metal target with high-energy electrons. These X-rays have wavelengths that are comparable to atomic spacings. X-rays are scattered by the surrounding electrons in the atmosphere of a crystalline substance. Atoms are always grouped in regular planes in crystals. As a result of the X-rays' interference with these planes, a diffraction pattern is produced.

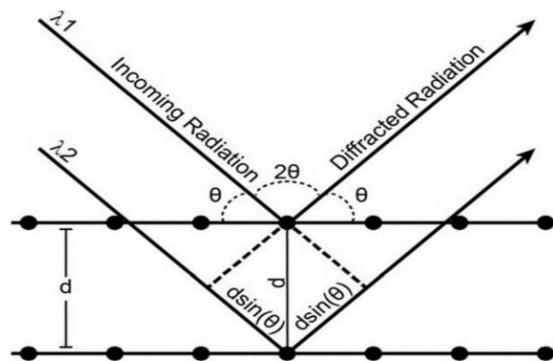


Figure 17. Schematic representation of Bragg's equation (Stan,18)

The main principle that explains this phenomenon is known as Bragg's law, which is as follows:  $n\lambda = 2d\sin\theta$ , where  $d$  is the distance of the atomic plane,  $\theta$  is the angle between the sample surface and the incoming X-ray beam,  $n$  is an integer, and  $\lambda$  is the wavelength of the incoming X-ray photons (Figure 17).

Powder X-ray diffraction is one of the many kinds of XRD techniques that are used for structural study and phase identification in polycrystalline materials (Figure 18).

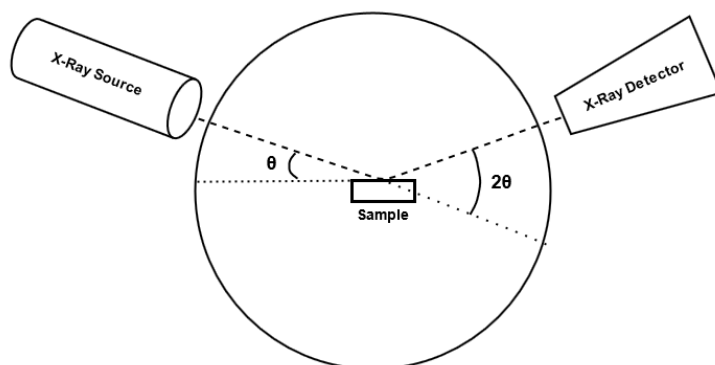


Figure 18. Schematic diagram of powder XRD

By gathering diffraction data at different angles, single-crystal X-ray diffraction can be used to ascertain the precise atomic structure of a single crystal. A more accurate version of XRD is called high-resolution X-ray diffraction, which is used to investigate semiconductor materials and epitaxial thin films.

The PANalytical EMPYREAN multipurpose X-ray diffractometer (PANalytical Almelo, The Netherlands) was used to measure the XRD patterns of the crystals and scaffolds. The diffractograms were measured from  $2\theta = 10^{\circ}$ - $80^{\circ}$  with a step of  $0.026^{\circ}$  using Ni-filtered Cu-K $\alpha$  radiation. Before the measurement, the crystals were ground into a powder.

## 2.3 Spectroscopic Properties

A Spectra 320 optical spectrum analyzer (Instrument Systems Optische Messtechnik GmbH, Germany) was used to record the upconversion spectra of the crystals and scaffolds that had been ground into powder. The UC spectra were captured between 350 and 700 nm in wavelength. A PROFILE Pro 808 nm laser driver supplied the excitation, and a Thorlab ITC 4020 temperature controller running at 1.25 A with an 808nm laser was used to regulate the temperature. The measurements were made at  $25^{\circ}\text{C}$  using an 808 nm laser. A Thorlabs ITC4001 laser diode/temperature controller was utilized for a 980 nm pump laser with a controlled temperature of  $30^{\circ}\text{C}$  and a current of 1A to compare the intensities of the powdered samples. Figure 19 shows the experimental setup of UC emission. The UC intensity and green afterglow from PeL were compared by using different laser pump power setups (808 nm and 980 nm) in a dark room with 2.5-12.5, 5-10, 7.5-7.5, 10-5 and 12.5-2.5 (which makes a total of 15 wt%) ratios of UC-PeL crystals. The distance between the excitation and the detector and the sample surface was 5 mm. To compare the intensity, the samples were ground into a powder

(Morales,20). Photons that are gathered by a detector are released when an electron relaxes in high-energy states via the radiation relaxation pathway. As seen below in Figure 20 (using as a reference), upconversion is based on a multiphoton process in

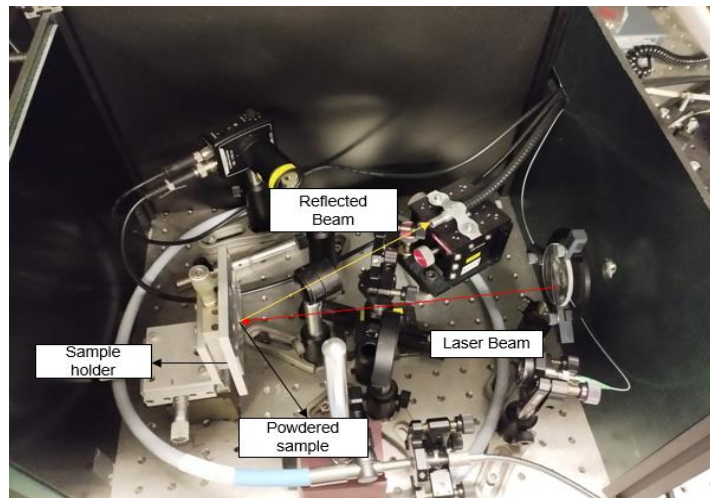


Figure 19. Experimental setup of UC emission

which an already excited electron gets further excited by a second photon before relaxing and emitting a photon of higher energy than the absorbed one. The radiative relaxation routes emit photons, which a detector then collects.

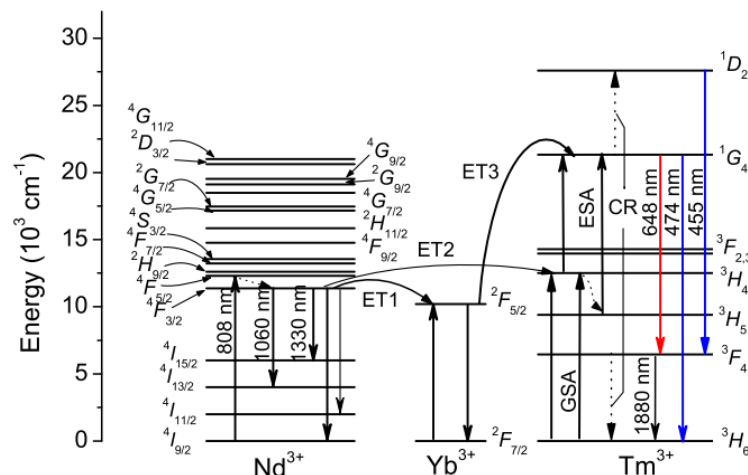


Figure 20. Energy level diagrams of Tm, Yb, Nd ions and the possible UC under 808 nm excitation (Tian,20)

To observe the afterglow, the bulk scaffold (sintered and unsintered) was charged by a compact UV lamp (UVGL-25, 4W,  $\lambda_{\text{exc}}$ : 254nm) for 5 minutes. The afterglow was examined in the dark to assess the scaffold's afterglow after charging. The powder Scaffolds (sintered and unsintered) were examined under 808 nm and 980 nm excitation in the dark to check the afterglow and blue UC emission from the samples.

## CHAPTER 3: RESULTS AND DISCUSSION

The fundamental purpose of this research is to develop an NIR-sensitive 3D printed biophotonic scaffold for bone healing, with the possibility to trigger light therapy, limiting the risk of infection, while promoting bone regeneration. The biophotonic scaffold should emit green afterglow after 808 nm charging. This can be achieved only with effective blue upconverter crystals. The current work focused on the development of the UC crystals and their integration into a printable bioactive ink for manufacturing biophotonic scaffolds.

### 3.1 Crystal Synthesis and Characterization

The main goal is the optimization of the RE concentration to prepare crystals with the proper crystalline phase and with strong blue UC under 808nm pumping.

#### 3.1.1 YPO<sub>4</sub> and CaWO<sub>4</sub> (Nd<sup>3+</sup>, Tm<sup>3+</sup>)

For this experiment, crystal preparation started with YPO<sub>4</sub>: Nd<sup>3+</sup>, Tm<sup>3+</sup>: [Y<sub>(1-x-y)</sub>PO<sub>4</sub>Nd<sub>x</sub>Tm<sub>y</sub>] co-doped with Nd<sup>3+</sup>, Tm<sup>3+</sup>. The concentration of Nd<sup>3+</sup> ranged from 0.5 to 25 at%, and that of Tm<sup>3+</sup> was 0.5 at%. The XRD pattern of the crystal is presented in Figure 21 (a). The XRD patterns of the as-prepared crystals exhibit peaks, the position of which corresponds well to those of the standard powder diffraction file entry 04-001-9248 of YPO<sub>4</sub>. Here, it shows the single phase of YPO<sub>4</sub> till 10 at% of Nd<sub>2</sub>O<sub>3</sub> content; after that, the second phase was detected.

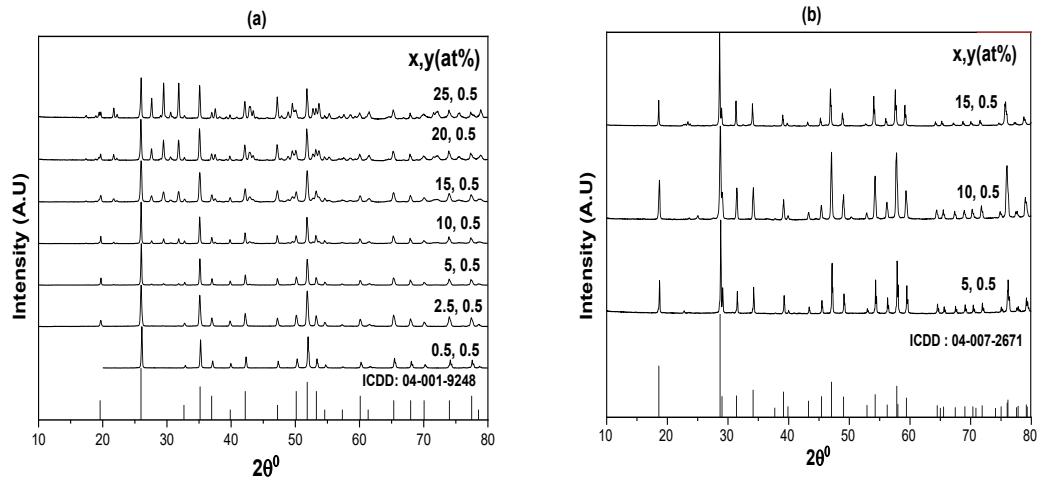


Figure 21. . (a) XRD patterns of the  $Y_{(1-x-y)}PO_4Nd_xTm_y$  crystals with different amount of  $Nd_2O_3$  and 0.5at% of  $Tm_2O_3$ ; (b) XRD of the  $Ca_{1-x-y-z}WO_4Nd_xTm_yNa_z$  crystals with different amount of  $Nd_2O_3$  and 0.5at% of  $Tm_2O_3$

Then,  $CaWO_4$ :  $[Ca_{1-2(x+y)}WO_4Nd_xTm_yNa_{(x+y)}]$  crystals were prepared with 0.5 at% of  $Tm_2O_3$  and the  $Nd_2O_3$  content ranging from 5 to 15 at% to optimize the  $Tm^{3+}/Nd^{3+}$  ratio. 20 at% and 25 at%  $Nd^{3+}$  remain unsuccessful as shown in Figure 22. The XRD patterns are presented in Figure 21 (b). It shows the crystals exhibit peaks, which are similar to the standard diffraction file entry 04-007-2671 of  $CaWO_4$  crystals.



Figure 22.  $Ca_{1-2(x+y)}WO_4Nd_xTm_yNa_{(x+y)}$  crystal (Nd 20at.%) difficult to extract

No up-conversion was detected from the crystals under 808 nm pump laser, as shown in Figure 23 (a) and (b).

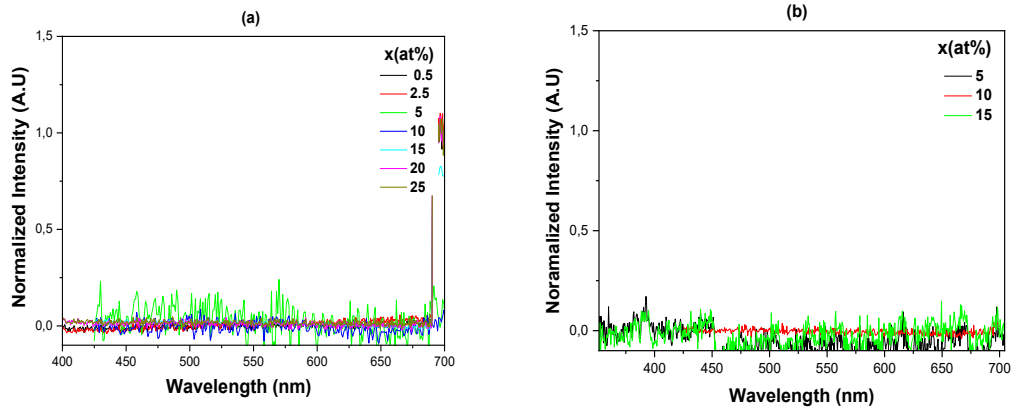


Figure 23. No upconversion at 808nm excitation codoped with  $\text{Nd}^{3+}/\text{Tm}^{3+}$  ions (a)  $\text{Y}_{(1-x-y)}\text{PO}_4\text{Nd}_x\text{Tm}_y$  crystals, (b)  $\text{Ca}_{1-2(x+y)}\text{WO}_4\text{Nd}_x\text{Tm}_y\text{Na}_{(x+y)}$  crystals

### 3.1.2 $\text{CaWO}_4$ ( $\text{Yb}^{3+}$ , $\text{Tm}^{3+}$ )

$\text{CaWO}_4$  :  $[\text{Ca}_{1-2(x+y)}\text{WO}_4\text{Yb}_x\text{Tm}_y\text{Na}_{(x+y)}]$  crystals were prepared with a  $\text{Tm}_2\text{O}_3$  content of 0.25 at.% and a  $\text{Yb}_2\text{O}_3$  content that ranges from 2.5 to 12.5 at.%. Then, the process continues with 7.5 at.%  $\text{Yb}_2\text{O}_3$  content with a different range of  $\text{Tm}_2\text{O}_3$  content (0.125 to 0.5at.%). Figure 24 (a) and (b) displays the crystals' XRD pattern. The prepared crystals' XRD patterns show peaks whose positions closely match those of standard powder diffraction file entry 04-007-2671 of  $\text{CaWO}_4$ . This indicates that the rare earth dopant ions replace  $\text{Ca}^{2+}$  because their ionic radii are similar: 112 p.m. for  $\text{Ca}^{2+}$ , 99.4 p.m. for  $\text{Tm}^{3+}$ , 98.5 p.m. for  $\text{Yb}^{3+}$  (Shanon,76), and 118 p.m. for  $\text{Na}^+$  (Magalhaes,23).

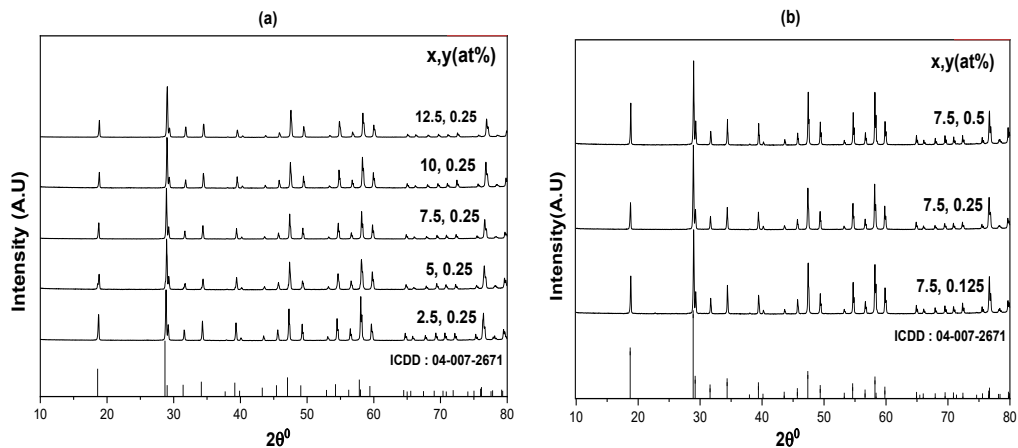


Figure 24. (a) XRD patterns of  $\text{Ca}_{1-2(x+y)}\text{WO}_4\text{Yb}_x\text{Tm}_y\text{Na}_{(x+y)}$  crystals prepared with different amounts of  $\text{Yb}_2\text{O}_3$  and 0.25 at% of  $\text{Tm}_2\text{O}_3$ ; (b) XRD patterns of  $\text{Ca}_{1-2(x+y)}\text{WO}_4\text{Yb}_x\text{Tm}_y\text{Na}_{(x+y)}$  crystals with 7.5 at%  $\text{Yb}_2\text{O}_3$  and different amounts of  $\text{Tm}_2\text{O}_3$

As the  $\text{Yb}_2\text{O}_3$  content rises, the XRD peaks move towards higher angles, indicating the structure has contracted as a result of the various ionic radii (Magalhaes,23). The successful charge compensation with  $\text{Na}^+$  is also indicated by the lack of any secondary phases. These crystals emitted blue light under 808 nm excitation, which was visible to the naked eye.

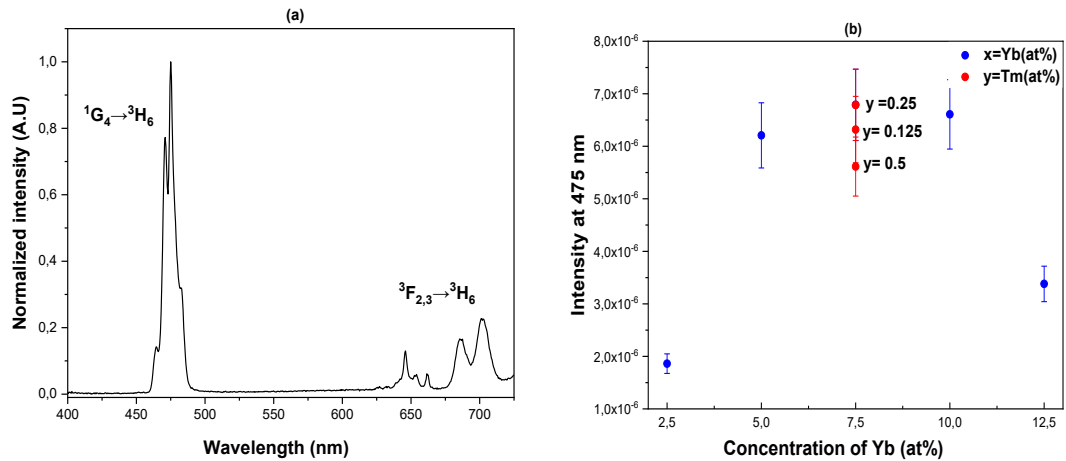


Figure 25. (a) Normalized upconversion spectrum of  $\text{Yb}_{x7.5}\text{Tm}_{y0.25}$  crystal, taken as an example. (b) Relative intensity of the blue emission at 475 nm as a function of  $\text{Yb}_2\text{O}_3$  at%(x) and  $\text{Tm}_2\text{O}_3$  at%(y) in the crystals ( $\lambda_{\text{exc}} = 808\text{nm}$ )

Under 808 nm excitation, the upconversion (UC) spectra from the  $\text{CaWO}_4$  crystal display two emission bands centered at 475 nm and 702 nm (Figure 25 a), which are characteristic of  $\text{Tm}^{3+}$  ions. These emissions correspond to the  $^1\text{G}_4 \rightarrow ^3\text{H}_6$  and  $^3\text{F}_{2,3} \rightarrow ^3\text{H}_6$  transitions of  $\text{Tm}^{3+}$  ions, respectively. As the concentration of  $\text{Yb}^{3+}$  increases, the intensity of all emission bands first increases and then decreases. (Figure 25 b) In the range of low concentration,  $\text{Yb}^{3+}$  ions can act as an excellent sensitizer for  $\text{Tm}^{3+}$  ions. So, the upconversion luminescence mechanism of  $\text{Tm}^{3+}$  ions in Yb/Tm co-doped  $\text{CaWO}_4$  crystals is expected to be ET (energy transfer) mixed with two- to three-photon processes (Ling,13). It is clearly shown that the concentration of Yb (7.5 at%) with fixed Tm (0.25 at%) concentration was found to have the highest blue upconversion.

Then the amount of  $\text{Tm}^{3+}$  was varied between 0.125 to 0.5 at% to further increase the intensity of the blue UC. 0.25 at% of  $\text{Tm}^{3+}$  was found to lead to strong blue emission. The XRD of the synthesized crystal  $\text{CaWO}_4: \text{Yb}^{3+}/\text{Tm}^{3+}$  can be seen in Figure 26b, where a single phase of  $\text{CaWO}_4$  (ICDD: 04-007-2671) was evident. From this data, the two contents of the highest intensities were chosen for the 3D printing (Yb7.5 to 10 at.% and Tm 0.125 to 0.25 at%).

### 3.1.3 CaWO<sub>4</sub> (Yb<sup>3+</sup>, Tm<sup>3+</sup>, Nd<sup>3+</sup>)

At this stage, CaWO<sub>4</sub> : Yb<sup>3+</sup>/Tm<sup>3+</sup>/Nd<sup>3+</sup>: [Ca<sub>1-2(x+y)-z</sub> WO<sub>4</sub>Yb<sub>x</sub>Tm<sub>y</sub>Nd<sub>z</sub>Na<sub>(x+y)</sub>] was triply doped with Yb<sup>3+</sup>, Tm<sup>3+</sup>, and Nd<sup>3+</sup>. According to some studies and experimental data, the doping concentration of Yb<sub>2</sub>O<sub>3</sub> and Tm<sub>2</sub>O<sub>3</sub> was respectively designed as 10 at% and 0.25 at% as this composition already successfully showed the highest intensity under 980nm excitation. (Maglhaes, 23). The doping concentration of Nd<sub>2</sub>O<sub>3</sub> varied from 0.125 to 5 at%. The XRD patterns of these crystals are depicted in Figure 26.

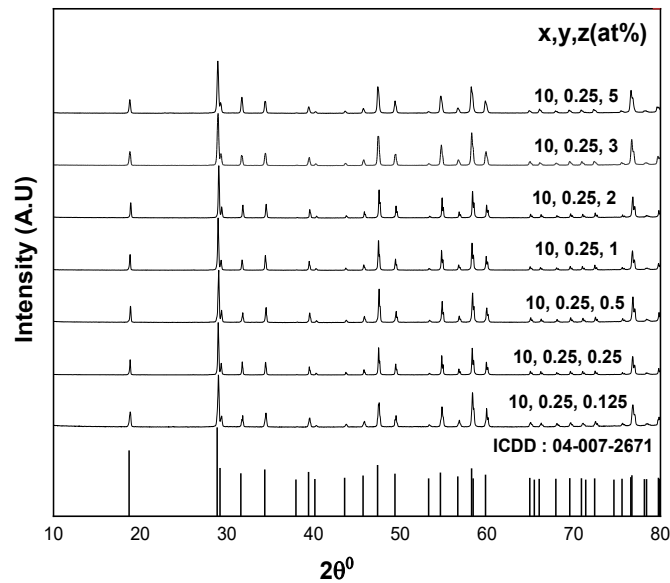


Figure 26. XRD patterns of the Ca<sub>1-2(x+y)-z</sub> WO<sub>4</sub>Yb<sub>x</sub>Tm<sub>y</sub>Nd<sub>z</sub>Na<sub>(x+y)</sub> with different amounts of Nd<sub>2</sub>O<sub>3</sub> with 10 at% Yb<sub>2</sub>O<sub>3</sub> & 0.25 at% Tm<sub>2</sub>O<sub>3</sub>

The XRD patterns show the peak related to CaWO<sub>4</sub> crystals confirming that the crystals can be triple doped. Changing the Nd<sup>3+</sup> doping level doesn't damage the host structure. The crystal structure is quite stable. The UC spectrum and the relative intensities of the crystals are shown in Figure 27 (a) and (b). The UC spectrum data show that the different concentrations of Nd<sup>3+</sup> ions (represented by different colors) do not change the shape of the emission bands. In Figure 27 (b), the highest blue emission is obtained from the crystals prepared with 0.25 at% of Nd<sup>3+</sup> before concentration quenching occurs for larger amount of Nd<sup>3+</sup>.

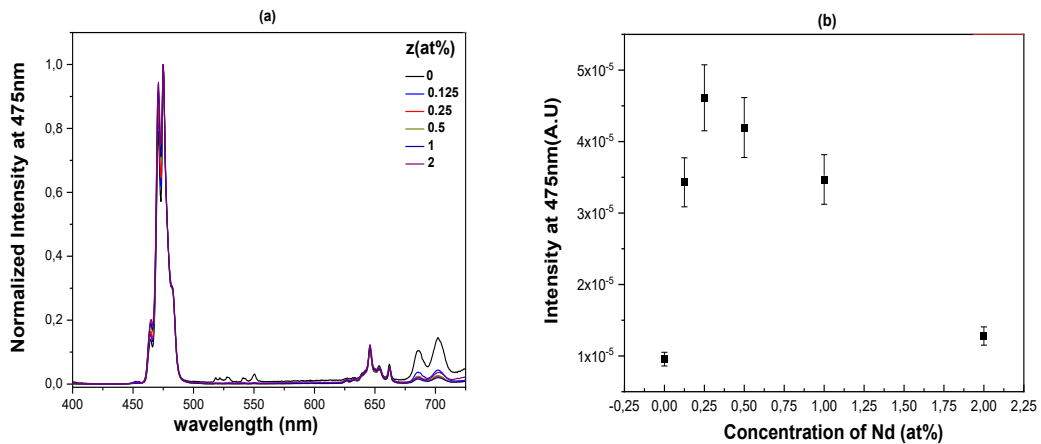


Figure 27. (a) Normalized UC spectrum of the  $\text{Yb}_x10, \text{Tm}_y0.25, \text{Nd}_z(0 \text{ to } 2) \text{ at\%}$  crystal  $\text{Ca}_{1-2(x+y)-z}\text{WO}_4\text{Yb}_x\text{Tm}_y\text{Nd}_z\text{Na}_{(x+y)}$ , (b) relative intensity of the blue emission at 475nm as a function of  $\text{Nd}_2\text{O}_3$  at% in the crystals ( $\lambda_{\text{exc}} = 808\text{nm}$ )

According to Figure 27.b, the best UC Crystal doped with 0.25 at%  $\text{Nd}^{3+}$ , 7.5 at%  $\text{Yb}^{3+}$  & 0.25 at%  $\text{Tm}^{3+}$  was chosen for 3D printing.

## 3.2 3D printing of Scaffolds

### 3.2.1 UC-PeL ratio optimization

In this section, different ratios of UC-PeL composites are introduced, which were optimized to obtain green PeL after 980 and 808 nm charging. After that optimization, the ink for scaffolds was prepared.

**Crystal without  $\text{Nd}^{3+}$ :** After the crystal ( $\text{CaWO}_4:\text{Yb}^{3+}/\text{Tm}^{3+}$ ) preparation, UC-PeL composites were prepared by manually adding 10 wt% and 15 wt% UC-PeL mix in the  $\text{NaPO}_3$  powder. These UC-PeL mixtures were prepared by adding 2.5 to 14 wt% of  $\text{CaWO}_4:[\text{Ca}_{1-2(x+y)}\text{WO}_4\text{Yb}_x\text{Tm}_y\text{Na}_{(x+y)}]$  crystal (co-doped with 7.5 at% of  $\text{Yb}_2\text{O}_3$  and 0.125 at% of  $\text{Tm}_2\text{O}_3$ ) and 1 to 7.5 wt% of  $\text{SrAl}_2\text{O}_4:\text{Eu}^{2+}, \text{Dy}^{3+}$  PeL Phosphors in 0.5 gram  $\text{NaPO}_3$ . To optimize UC-PeL composites, 808 nm and 980 nm pump lasers were used. After 5 minutes of charging, the composites showed a very weak afterglow in 808 nm, but under 980 nm, they showed a strong green afterglow. Figure 28 (a) and (b) depict the intensities of the UC-PeL crystals under 808 nm and 980 nm excitation.

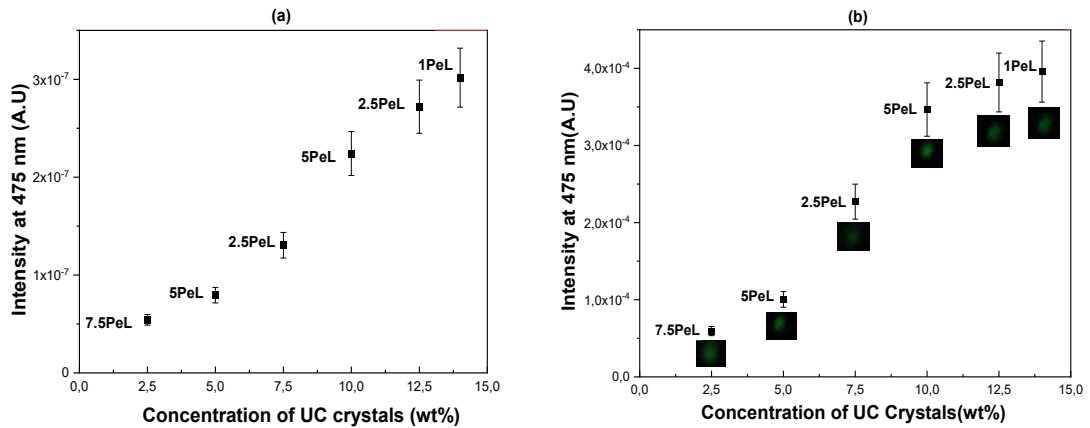


Figure 28. Intensity of UC-PeL crystals without  $\text{Nd}^{3+}$  different concentrations of UC crystal and PeL (a) in 808 nm laser pump with weak afterglow; (b) in 980 nm laser pump, strong green afterglow.

In Figure 28, the intensity of the blue emission under 808 and 980 nm lasers increases with an increase in the wt% of the UC crystals. More importantly, the 980 nm excitation offers more efficient upconversion performance. 808 nm excitation results in much weaker upconversion. While green PeL could be seen after 980 nm charging, very weak green afterglow could be seen after 808nm charging. The differences stem from the excitation pathways because of 980 nm directly driving the  $\text{Yb}^{3+}/\text{Tm}^{3+}$  upconversion process with high efficiency, where 808 nm usually relies on  $\text{Nd}^{3+}$  sensitization (Wing,22). Figure 28 b shows the minimum intensity of the blue emission, which should be achieved to charge the PeL phosphors. Low UC concentrations (less than 5wt % of UC crystals) are too weak to populate the traps in the persistent phosphor significantly. But at higher UC concentrations (10–15%), the upconversion intensity at 475 nm became sufficient to excite the phosphor and produce a noticeable green glow after excitation. In practical terms, the sample crosses a threshold where NIR charging is effective: enough blue/UV light is generated to induce persistent luminescence. This threshold corresponds with the higher end of UC loading in the experiment. It is consistent with findings in NIR-charged persistent phosphor composites, where only above a certain UC output (or certain  $\text{Yb}^{3+}/\text{Tm}^{3+}$  doping level) is the energy transfer enough to yield visible afterglow. (Arango,22). Some studies demonstrated that by combining  $\text{Yb}^{3+}/\text{Tm}^{3+}$  upconverters with  $\text{SrAl}_2\text{O}_4:\text{Eu, Dy}$ , one can achieve green afterglow after 980nm excitation, but the afterglow brightness and duration increase with the amount of persistent phosphor available to capture the UC emission. (Arango,22). In this case, all samples contained some PeL phosphor, and by 12.5–15 wt% UC (with 2.5–1 wt% PeL), the blue output was intense enough to charge even that small amount of PeL, yielding a visible afterglow.

had the PeL fraction been larger at high UC, the afterglow might have been even stronger.

Here, the best two composites: 10 wt%UC-5 wt%PeL and 14 wt%UC-1 wt%PeL were chosen for 3D printing.

**Crystal with  $\text{Nd}^{3+}$ :** UC-PeL composites were prepared by adding 15 wt% UC-PeL in  $\text{NaPO}_3$  Powder. Where UC-PeL mix was prepared by adding 2.5 to 12.5 wt%  $\text{CaWO}_4$ :  $[\text{Ca}_{1-2(x+y)-z}\text{WO}_4\text{Yb}_x\text{Tm}_y\text{Nd}_z\text{Na}_{(x+y)}]$  crystal (tri-doped with 10 at% of  $\text{Yb}_2\text{O}_3$ , 0.25 at% of  $\text{Tm}_2\text{O}_3$  and 0.25 at% of  $\text{Nd}_2\text{O}_3$ ) and 2.5 to 12.5 wt%  $\text{SrAl}_2\text{O}_4$ :  $\text{Eu}^{2+}$ ,  $\text{Dy}^{3+}$  PeL Phosphors in 0.5g  $\text{NaPO}_3$  powder.

808 nm and 980nm both excitations are used to optimize these UC-PeL crystals (same procedure as the 1<sup>st</sup> part.). As for the other crystals, the mixtures showed very weak afterglow after being charged for 30 minutes with 808nm (Figure 29 a), but they luminated a strong green afterglow after being charged for 5 minutes with 980 nm (Figure 29 b). Here, the best UC-PeL combination (5 wt% UC-10 wt% PeL) and (7.5 wt% UC-7.5 wt% PeL) were chosen for the 3D printing.

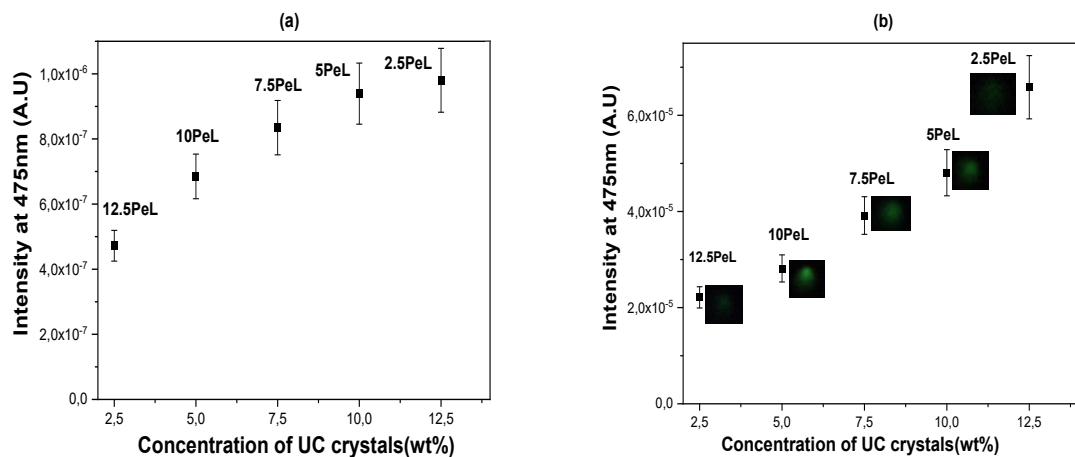


Figure 29. Intensity of UC-PeL crystals with  $\text{Nd}^{3+}$  different concentrations of UC & PeL (a) in 808 nm (b) in 980 nm excitation

### 3.2.2 3D Printed Scaffolds and Characterization

**Crystal without  $\text{Nd}^{3+}$ :** In the initial stage of the 3D scaffold printing process, the ink is prepared with a precise composition. This ink consists of 1393B20 bioactive glass powder (85 wt%) and UC-PeL components as explained in section §2.1.3 which are (1 wt%UC–14 wt% %PeL), and (10 wt%UC–5 wt%PeL). A Pluronic F-127 binder (30 wt% aqueous solution) is added to the mixture to ensure a suitable viscosity for printing. The printed scaffold was a cylindrical porous shape with a 6 mm diameter and 2.5 mm height. Green afterglow was seen from all scaffold samples after UV charging. Sintered ones showed lighter afterglow compared to unsintered ones, which confirms that the PeL particles lost their brightness on the scaffold after sintering (Figure 30). After sintering, it was qualitatively observed that they became denser, brittle, and smoother with slight shrinkage.

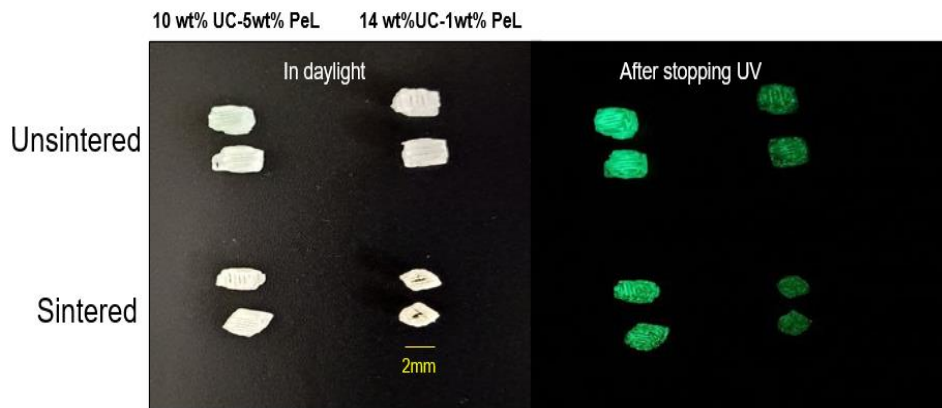


Figure 30. Picture of unsintered and sintered scaffolds without  $\text{Nd}^{3+}$  in daylight, and after UV charging

The XRD patterns of the sintered and unsintered scaffolds (Figure 31) confirmed the presence of crystalline  $\text{CaWO}_4$ .

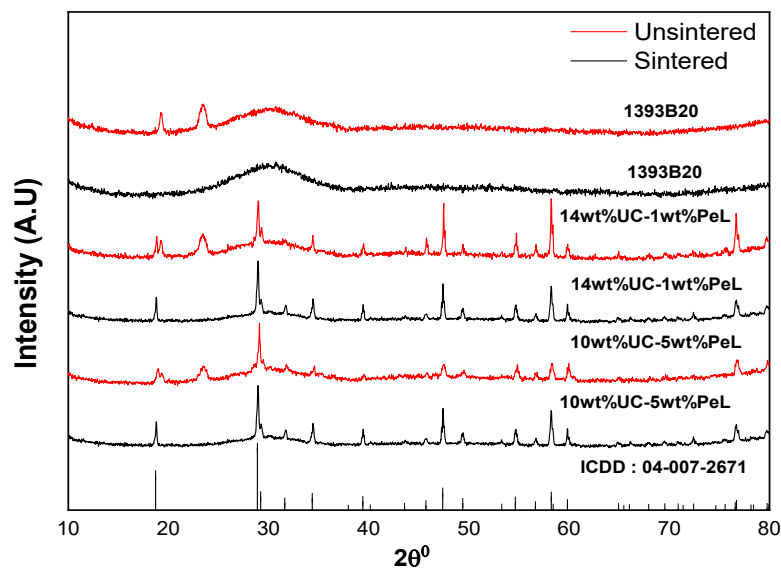


Figure 31. XRD patterns of sintered-unsintered scaffold and 1393B20 glass powder.

Sintered samples exhibited sharper and more intense peaks compared to unsintered ones. The 14 wt%UC-1 wt% PeL composition, with higher  $\text{CaWO}_4$  content, showed more intense peaks than the 10 wt%UC-5 wt%PeL sample, reflecting the greater proportion of crystalline phase. No distinct peaks were attributed to the PeL component, due to its low concentration. The 1393B20 glass (top two patterns) displays a broad amorphous humps centered around  $25\text{--}35^\circ$ , to Figure 31. The unsintered scaffolds showed two peaks at  $20\text{--}30^\circ$ , which were attributed to the crystallinity of Pluronic (Pawar,16). The amorphous structure remains unchanged after sintering, confirming that the glass phase retains its amorphous nature and does not crystallize during heat treatment, which is a desirable property for maintaining bioactivity and ion release. (Szczodra,24 b).

Figure 32 (a) and (b) show the intensity of the blue emission from the sintered and unsintered scaffolds under excitation at 808 nm and 980nm.

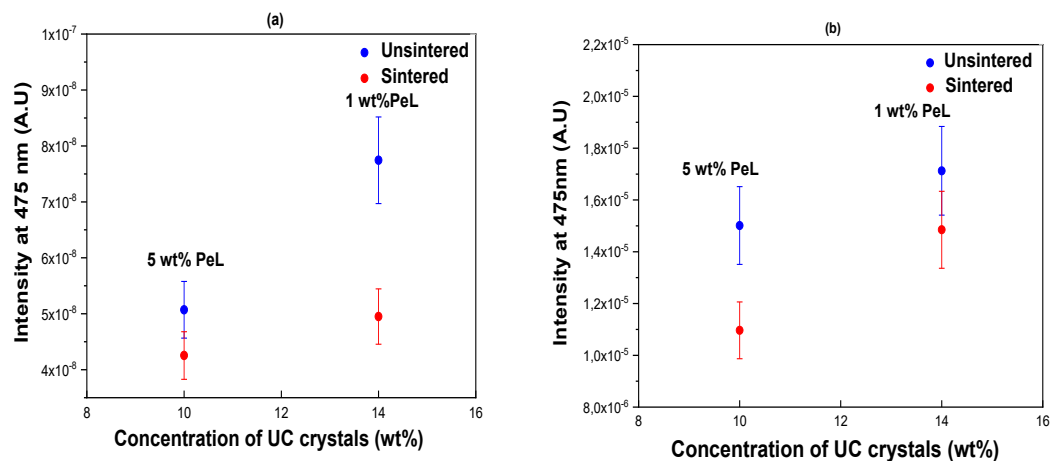


Figure 32. Relative Intensity of Sintered and Unsintered scaffold without  $\text{Nd}^{3+}$  doped crystal (a) in 808 nm excitation (b) in 980 nm excitation

A decrease in the intensity of the blue emission is observed after sintering probably due to the formation of defects occurring during the sintering step as reported in (Magalães, 25)

**Crystal with Nd<sup>3+</sup>:** 3D printed composite scaffold was prepared using UC crystal CaWO<sub>4</sub>: [Ca<sub>1-2(x+y)-z</sub>WO<sub>4</sub>Yb<sub>x</sub>Tm<sub>y</sub>Nd<sub>z</sub>Na<sub>(x+y)</sub>]. The ink consists of 1393B20 powder (85 wt%), and two UC-PeL components are (5 wt%UC–10 wt%PeL), and (7.5 wt%UC–7.5 wt%PeL). The scaffolds' dimensions were similar to those explained in the previous section. Overall, the ink seemed to be capable of 3D printing. Some of the printed scaffolds were sintered as explained in §2.1.3. for comparison. Upon 5-minute UV charging, the 7.5 wt% UC sample showed brighter afterglow than the 5 wt% UC (Figure 33).

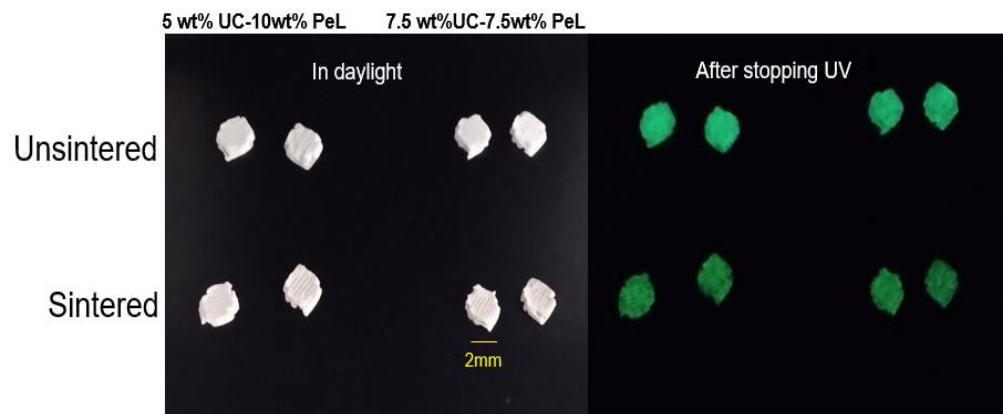
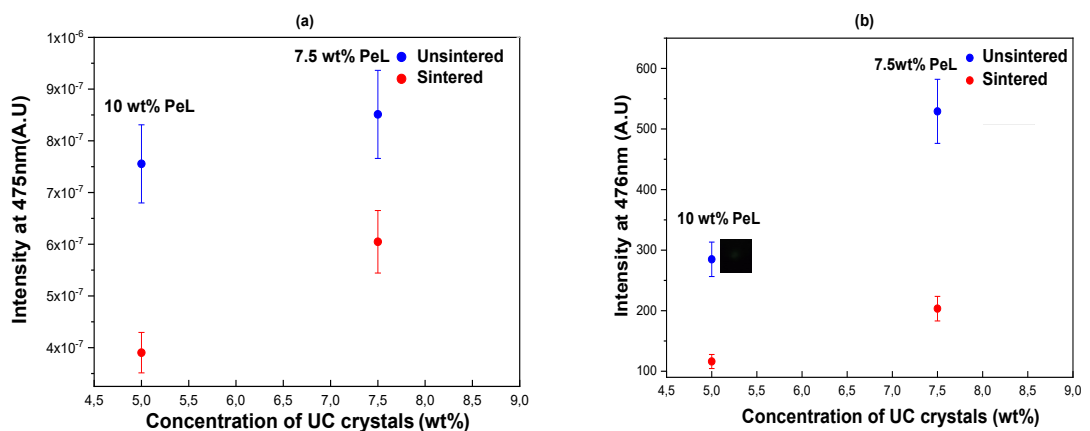


Figure 33. Pictures of Sintered and Unsintered scaffolds in daylight and after UV charging

In Figure 34 (a) and (b), it can be clearly seen that the sintering process also affects the blue UC luminescence and green afterglow, as it reduced the blue luminescence from  $7.5 \times 10^{-7}$  to  $4 \times 10^{-7}$  nm, which is 47% (for 5 wt% UC-10 wt% PeL) and from  $8.5 \times 10^{-7}$  to  $6 \times 10^{-7}$  nm, which is 30% (for 7.5 wt%UC-7.5 wt% PeL) in 808 excitation. Similarly, in 980 nm the luminescence reduced 36% for 5 wt% UC-10 wt% PeL concentration and 64% for 7.5 wt%UC-7.5 wt% PeL concentration.



*Figure 34. Relative Intensity of Sintered and Unsintered Scaffold with  $\text{Yb}^{3+}/\text{Tm}^{3+}/\text{Nd}^{3+}$  doped crystal (a) in 808nm (b) in 980nm*

Green afterglow was seen from the 5 wt%UC-10 wt%PeL after 980 nm charging. This scaffolds also emits a weak green afterglow in 808 nm, seen by the naked eye.

By comparing printability and luminescence, the  $\text{CaWO}_4$  crystal, tri-doped with 10 at%Yb, 0.25 at%Tm, 0.25 at% Nd, has shown the highest blue intensity under 808 nm excitation. For future studies, more 3D printed scaffolds (without PeL) could be prepared by using this upconverted crystal, to observe how the blue intensity works without the PeL particle under 808 nm.

## CONCLUSIONS

In summary, within this work, blue upconverter crystals were successfully developed and their RE concentration optimized to achieve the strongest blue emission. The newly developed crystals were integrated into biophotonic 3D-printed scaffolds for bone healing applications. The goal was to develop photosensitive and luminescent printable scaffolds that are capable of converting NIR to long-lasting green light suitable for implantation and optical monitoring.

YPO<sub>4</sub> and CaWO<sub>4</sub> crystals doped with Nd<sup>3+</sup> and Tm<sup>3+</sup> ions were synthesized and characterized. Both YPO<sub>4</sub> and CaWO<sub>4</sub> failed to display blue emission under 808 nm excitation. For an improvement of the optical properties fitting the purpose, CaWO<sub>4</sub> crystals were co-doped with Yb<sup>3+</sup> and Tm<sup>3+</sup> ions. This composition showed strong blue upconversion emission at 475 nm and weaker red emission near 702 nm under 808 nm excitation. The highest blue emission in CaWO<sub>4</sub> crystals co-doped with Yb<sup>3+</sup> and Tm<sup>3+</sup> was achieved with 7.5 to 10 at% of Yb<sup>3+</sup> and 0.25 at% of Tm<sup>3+</sup>, which demonstrates an efficient energy transfer process between Yb<sup>3+</sup> and Tm<sup>3+</sup>.

To increase further sensitivity to NIR, CaWO<sub>4</sub> was triply doped with Yb<sup>3+</sup>, Tm<sup>3+</sup>, and Nd<sup>3+</sup> ions. This tri-doped composition, containing 10 at% Yb<sup>3+</sup>, 0.25 at% Tm<sup>3+</sup>, and 0.25 at% Nd<sup>3+</sup> ions, exhibited the highest blue emission in 808 nm excitation. However, higher Nd<sup>3+</sup> concentrations led to concentration quenching, reduced intensity. These results showed that dopant ratios are crucial for balancing energy transfer efficiency and, therefore, tailoring the optical properties of the materials.

Successively, the best UC crystals (which showed the highest emission at 808 nm) were combined into UC–PeL (persistent luminescent) composites by using NaPO<sub>3</sub> powder. Under 980 nm excitation, these composites exhibited intense and long-lasting green afterglow. On the other hand, 808 nm excitation produced only weak afterglow. The composites were subsequently integrated into 1393B20 bioactive glass for 3D printing of cylindrical porous scaffolds. After sintering, the scaffolds preserved their structural integrity, porosity, and photoluminescent properties, but with a little bit reduction in emission intensity. Among all samples, scaffolds prepared with CaWO<sub>4</sub>:(Yb<sup>3+</sup>, Tm<sup>3+</sup>, Nd<sup>3+</sup>) displayed the best printability and strongest NIR-induced luminescence.

This research showed an effective way to create NIR-excitable and bioactive 3D-printed scaffolds, which has been prepared from blue upconverter and green persistent luminescent phosphors as a dispersed phase within a continuous BAG matrix. These

scaffolds combine optical functionality with the ability to be 3D printed and successfully sintered into the shape of interest. The optical properties of the material open wide perspectives for the applicability in light therapies, for example, to limit the risk of infections.

As for the next steps, a wider physicochemical characterization of the scaffolds should be performed, including the evaluation of their bioactivity and mechanical properties, as well as the characterization of their biological response, both *in vitro* and, later, *in vivo*, assessing the cyto- and biocompatibility of the material and its osteogenic properties. Future studies should also focus on improving the upconversion efficiency at 808 nm by changing ratios of PeL phosphors for long-lasting green afterglow. More 3D printed scaffolds (without PeL) could be prepared by using this upconverted crystal, to observe how the blue intensity works without the PeL particle under 808nm. Additionally, investigating only UC crystal scaffolds without PeL particles and glass powder could further clarify the role of pure upconverted emission in tissue stimulation and optical sensing.

## REFERENCES

(Abdelghany,13) : A.M.Abelghany; Spectrochimica Acta Part A: Molecular & Biomolecular Spectroscopy; 2013, 100,120-126.

Available: <https://doi.org/10.1016/j.saa.2012.02.051>

(Aljaman,25) : M.Aljaman, M.H.A.Mhareb, A.Mekki, E.Kotb, N.Alonizan, M.Y.Alqahtani, H.Almarri, I. Biag; Bioactive properties for borate and borosilicate glass: An *in vitro* study; Journal of Non-Crystalline Solids, X, 2025, 26,100222.

Available: <https://doi.org/10.1016/j.nocx.2025.100222>

(Arango,22) : N.G.Arango, S Vuori, H.Byron, D.V.D.Heggen, P.F.Smet, M.Lastusecari, L.Petit; Near-Infrared rechargeable glass-based composites for green persistent Luminescence; Journal of Alloys and Compounds; 2022, 927,167048.

Available: <https://doi.org/10.1016/j.jallcom.2022.167048>

(Ananth,24) : K.P.Ananth, N.D.Jayram; A comprehensive review of 3D printing techniques for bio-material based scaffold fabrication in bone tissue engineering, Annals of 3D Printed Medicine; 2024, 13, 100141.

Available: <https://doi.org/10.1016/j.stlm.2023.100141>

(Azad,20): M.A.Azad, D.Olawuni, G.Kimbell, A.Z.Md Badruddoza, M.S.Hossain, T.Sultana; Polymers for extrusion-based 3D printing of pharmaceutical: A holistic materials process perspective; 3D Printing of Pharmaceuticals and Drug Delivery Devices, MDPI; 2020,12 (2),124.

Available: <https://doi.org/10.3390/pharmaceutics12020124>

(Bajestani,23) : M.M.Bajestani, A.H.Bahmanpour, M.Ghaffori, F.Moztarzadeh, A.Sepahvandi, K.Adebajo; Reviewing the bio-applications of SrAl<sub>2</sub>O<sub>4</sub>: Eu<sup>2+</sup>, Dy<sup>3+</sup> phosphor; Journal of Biology and Medicine,2023, 7 (1), 44-52.

Available: <https://doi.org/10.17352/jbm.000040>

(Balaram,19) : V.Balaram; Rare earth elements: A review of applications, occurrence, exploration, analysis, recycling and environmental impact; Geoscience Frontiers; 2019, 10 (4),1285-1303.

Available: <https://doi.org/10.1016/j.gsf.2018.12.005>

(Binnemans,09): K.Binnemans; Lanthanide-based luminescent hybrid materials; Chemical Reviews; 2009,109 (9), 4283-4374.

Available: <https://doi.org/10.1021/cr8003983>

(Brito,12) : H.F.Brito, J.Holsa, T.Laamanen, M.Lastusaari, M.Malkamaki, L.C.V.Rodrigues; Persistent Luminescence mechanisms: human imagination at work; Optical Materials Express; 2012, 2 (4), 371-381.

Available: <https://doi.org/10.1364/OME.2.000371>

(Cannio,21) : M.Cannio, D.Bellucci, J. A.Roether, D.N.Baccaccini, V.Cannillo; Bioactive glass applications: A literature review of human clinical trials; Materials, MDPI; 2021, 14 (18), 5440.

Available: <https://doi.org/10.3390/ma14185440>

(Chan,17) : M.H.Chan, Y.T.Pan, I.J.Lee, C.W.Chen, Y.C.Chan, M.Hsiao, F.Wang, L.Sun, X.Chen; Minimizing the Heat effect of Photodynamic therapy based on inorganic Nano composites mediated by 808nm Near-Infrared light; Small; 2017, 13 (21), 1700038.

Available: <https://doi.org/10.1002/sml.201700038>

(Chavez,06): J.J.E.Chavez, M.L.Cervantes, A.Naik,Y.Kalia, D.Quintaner, A.Ganem; Applications of thermo-reversible pluronic F-127 gels in pharmaceutical formulations; Journal of Pharmacy and Pharmaceutical Sciences; 2006, 9 (3), 339-358.

Available: <https://archive-ouverte.unige.ch/unige:22653>

(Cullity,78) : B.D.Cullity, Chapter 1. Properties of X-Rays, Elements of X-ray Diffraction, 2<sup>nd</sup> edition; 1978, 1-30.

Available:

[https://www.eng.uc.edu/~beaucag/Classes/AdvancedMaterialsThermodynamics/Books/B.D.%20Cullity,%20S.R.%20Stock%20-%20Elements%20of%20X-Ray%20Diffraction-Pearson%20Education%20Limited%20\(2014\).pdf](https://www.eng.uc.edu/~beaucag/Classes/AdvancedMaterialsThermodynamics/Books/B.D.%20Cullity,%20S.R.%20Stock%20-%20Elements%20of%20X-Ray%20Diffraction-Pearson%20Education%20Limited%20(2014).pdf)

(Deraine,21) : A. Deraine ,M.T.R. Calejo, R. Agnicl,M. Kellomaki, E.Pauthe, M.Boissiere, and J.Massera; Polymer-Based Honeycomb Films on Bioactive Glass: Toward a Biphasic Material for Bone Tissue Engineering Applications; Applied Materials and Interfaces; 2021,13 (25), 29984-29995.

Available: <https://doi.org/10.1021/acsami.1c03759>

(E.Tech.Resources,21) : E.Tech. Resources;2021. (Visited March 2025)

Available: <https://rareearthexploration.com/what-are-rare-earth-elements-rees-where-are-they-found-and-how-are-they-mined/>

(Faber,17) : M.Fabert, N.Ojha, E.Erasmus, M.Hannula, M.Hokka, J.Hyttinen, J.Rocherulle, J.Sigalas, J.Massera; Crystallization and sintering of borosilicate bioactive glasses for application in tissue engineering; Journal of Materials Chemistry B; 2017,5 (23), 4514-4525.

Available: <https://doi.org/10.1039/C7TB00106A>

(Fagerlund,12): S. Fagerlund; Understanding the *in vitro* Dissolution Rate of Glasses with Respect to Future Clinical Applications, Academic Dissertation, Abo Akademi University; 2012, ISBN 978-952-12-2814-8.

Available:<https://www.doria.fi/handle/10024/85106>

(Francisco,21) : L.H.C.Francisco, R.P.Moreira, M.C.F.C.Felinto, V.C.Teixeira, H.F.Brito, O.L.Malta; SrAl<sub>2</sub>O<sub>4</sub> :Eu<sup>2+</sup>, Dy<sup>3+</sup> persistent luminescent materials functionalized with the Eu<sup>3+</sup> (TTA)-complex by microwave-assisted method; Journal of Alloys and Compounds; 2021, 882 (15), 160608.

Available:<https://doi.org/10.1016/j.jallcom.2021.160608>

(Fu,10) : Q.Fu, M.N.Rahaman, B.S.Bal, L.F.Bonewald, K.Kuroki, R.F.Brown; Silicate, borosilicate and borate bioactive glass scaffolds with controllable rate for bone tissue engineering applications II. *In vitro* and *in vivo* biological evaluation; Journal of Biomedical Materials Research part A; 2010, 95A (1), 172-179.

Available: <https://doi.org/10.1002/jbm.a.32823>

(Ghomi,12): H.Ghomi, M.H.Fathi, H.Edris; Effect of the composition of hydroxyapatite/bioactive glass nanocomposite foams on their bioactivity and mechanical properties; Journal of Materials Research Bulletin; 2012, 47(11); 3523-3532.

Available:<https://doi.org/10.1016/j.materresbull.2012.06.066>

(Gosen,17) :B.S.V.Gosen, P.L.Verplanck, R.R Seal, K.R.Long, J.Gambogi; Rare earth elements; 2017,1802, 1-31.

Available:<https://doi.org/10.3133/pp1802O>

(Groll,16) : J.Groll, T.Boland, T. Blunk, J.A Burdick, D.W.Cho, P.D. Dalton, B.Derby, G.Forgacs, Q.Li, V.A.Mironov, L.Moroni, M.Nakamura, W.Shu, S.Takeuchi, G.Vozzi, T.B.Woodfield, T.Xu, J.J.Yoo, J.Malda; Biofabrication: reappraising the definition of an evolving field; Biofabrication; 2016, 8 (1), 13001.

Available: <https://doi.org/10.1088/1758-5090/8/1/013001>

(Gu,12) : Y.Y.Gu, G.X.Wu,H.Lu, Y.Cui, H.Wang; High power diode laser for processing; Advanced Material Research; 2012, 472, 2508-2513.

Available: <https://doi.org/10.4028/www.scientific.net/AMR.472-475.2508>

(Hankenson,11) : K.D.Hankenson, M.Dishowitz, C.Gray, M.Schenker; Angiogenesis in bone regeneration; Injury; 2011, 42 (6), 556-561.

Available: <https://doi.org/10.1016/j.injury.2011.03.035>

(Hench,06) : L.L.Hench; The story of bioglass®, Journal of Materials Science: Materials in Medicine ; 2006, 17, 967-978.

Available: <https://doi.org/10.1007/s10856-006-0432-z>

(Hench,16) : L.L.Hench; Bioglass: 10 milestones from concept to commerce; Journal of Non-Crystalline Solids; 2016, 432A, 2-8.

Available: <https://doi.org/10.1016/j.jnoncrysol.2014.12.038>

(Hudson,13) : D.E. Hudson, D.O., Hudson, J.M. Winger, B.D.Richardson; Penetration of laser light at 808 nm and 980 nm in bovine tissue sample; Photomedicin and Laser Surgery; 2013, 31 (4), 163-168.

Available: <https://doi.org/10.1089/pho.2012.3284>

(Huang,24) : R.Huang, N.Ni,Y.Su, L.Gu, Y.Ju, D.Zhang, J.Li, M.Chang, Y.Chen, P.Gu, X.Fan; Chargeable persistent luminescence 3D printed scaffolds: a stepwise tactic for osteosarcoma treatment; Chemical Engineering Journal; 2024, 479, 147436.

Available : <https://doi.org/10.1016/j.cej.2023.147436>

(Jones,08) : J.R. Jones, Chapter 12 : Bioactive Glass; Bioceramics and their Clinical Applications; 2008, 266-283.

Available: <https://doi.org/10.1533/9781845694227.2.266>

(Jones,09) : J.R.Jones; New trends in bioactive scaffold: the importance of nanostructure; Journal of the European Ceramic Society; 2009, 29 (7), 1275-1281.

Available: <https://doi.org/10.1016/j.jeurceramsoc.2008.08.003>

(Kiselevskiy,23) : M.V.Kiselevskiy, N.Y.Anisimova, A.V.Kaupustin, A.A.Ryzhkin, D.N.Kuznetsova, V.V.Polyakava, N.A.Enikeev; Development of bioactive scaffold for orthopedic applications by designing additively manufactured Titanium porous structure; a critical review; Biomimetics, MDPI; 2023, 8 (7), 546.

Available: <https://doi.org/10.3390/biomimetics8070546>

(Li,20) : X. Li, B. Liu, B. Pei, J. Chen, D. Zhou, J Peng, X.Zhang, W.Jia, T Xu; Inkjet Bioprinting of Biomaterials; Chem Rev; 2020,120 (19), 10793–10833.

Available: <https://doi/10.1021/acs.chemrev.0c00008>

(Ling,13) : X.Y.Ling, W.Y.Long,S.L.Sheng, T.Xiang; Blue upconversion luminescence in Tm<sup>3+</sup>/Yb<sup>3+</sup> co-doped CaWO<sub>4</sub> polycrystals; Chinese Physics Letter; 2013, 30 (8), 084207..

Available: <https://doi/10.1088/0256-307X/30/8/084207>

(Liu,22) : N.Liu, X.Zhang, Q.Guo, T.Wu, and Y.Wang; 3D Bioprinted scaffold for tissue repair and regeneration; Frontiers in Materials;2022, 9, 925321.

Available: <https://doi.org/10.3389/fmats.2022.925321>

(Liu,25) : W.Liu, N.Cheong, Z.He, T.Zhang, Application of hydroxyapatite composites in bone tissue engineering: A review, Journal of Functional Biomaterials; 2025, 16 (4),127.

Available: <https://doi.org/10.3390/jfb16040127>

(Magalhaes,23) : E. S Magalhaes, A.Sedda, B.Bondzior, S.Vuori, D.V.D.Heggen, P.F.Smet, M.Lastussari, L.petit; Glass-based composites of CaWO<sub>4</sub>: Yb<sup>3+</sup>, Tm<sup>3+</sup> crystals and SrAl<sub>2</sub>O<sub>4</sub>: Eu<sup>2+</sup>, Dy<sup>3+</sup> phosphors for green afterglow after NIR charging; Ceramic International; 2023, 49 (24), 41150-41157.

Available: <https://doi.org/10.1016/j.ceramint.2023.01.155>

(Magalhaes,25) : E.S.Magalhaes, N.Ojha, S.Ghanavati, E.Opar, P.F.Smet, M.Lastusaari, F.Riefolo, C.Matera, J.Massera, P.Gorostiza, L.Petit; 3D printed glass-based biophotonic scaffolds for *in situ* activation of photoswitchable drugs; Journal of European Ceramic Society; 2025, 46, (2), 117777.

Available: <https://doi.org/10.1016/j.jeurceramsoc.2025.117777>

(Mancuso,17) : E.Mancuso, O.Bretcanu, M.Marshall, K.W.Dalgarno; Sensitivity of novel silicate and borate-based glass structure on *in vitro* bioactivity and degradation behavior; Ceramics International; 2017, 43 (15), 12651-12657.

Available : <https://doi.org/10.1016/j.ceramint.2017.06.146>

(Morales,20): G.A. Morales; Biophotonics Scaffolds for drug release using NIR excitation, Master's Thesis, Tampere University, 2020.

Available: <https://urn.fi/URN:NBN:fi:tuni-202004243663>

(Naraghi,13) : S.B.S.Naraghi, K.L.Christman; Chapter 3: Tissue engineering and the role of biomedical scaffolds: The evaluation of cardiac tissue engineering; Resident stem cells and Regenerative therapy; 2013, 43-67.

Available: <https://doi.org/10.1016/B978-0-12-416012-5.00003-7>

(Ning,17) : L.Ning and X.Chen,2017; A brief review of extrusion-based tissue scaffold bio-printing; Biotechnology Journal; 2017,12 (8), 1600671.

Available: <https://doi.org/10.1002/biot.201600671>

(Ojha,18) : N.Ojha, T. Laihinen, T.Salminen, M.Lastusaari, L.Petit; Influence of the phosphate glass melt on the corrosion of functional particles occurring during the preparation of glass-ceramics; Ceramics International; 2018, 44 (10), 11807-11811.

Available: <https://doi.org/10.1016/j.ceramint.2018.03.267>

(Ozkerim,18) : P.S.G.Ozkerim, I.Inci, Y.S.Zhang, A.Khademhosseini, M.R.Dokmeci; Bioinks for 3D bioprinting: an overview; Biomaterials Science ; 2018,6(5), 915-946

Available: <https://doi.org/10.1039/C7BM00765E>

(Pawar,17) : P.Pawar, S.Munishwar, S. Gautam, R.Gedam; Physical, thermal, structural, and optical properties of Dy<sup>3+</sup> doped lithium alumino-borate glasses for bright W-LED, Journal of Luminescence; 2017, 183, 79-88.

Available: : <http://dx.doi.org/10.1016/j.jlumin.2016.11.027>

(Prajzler,10) : V.Prajzler, O.Lyutakov, I.Huttel, J Oswald, V.Jerabek; Chapter 3 : Optical and spectroscopic properties of polymer layers doped with rare earth ions; Edited volume of Advances in Lasers and Electro Optics; 2010, 59-68.

Available:<https://doi.org/10.5772/8653>

(Rahaman,11) : M.N.Rahaman,D. E. Day, B.S.Bal, Q.Fa, S.B.Jung, L.F.Bonewald, A.P.Tomsia; Bioactive glass in tissue engineering; Acta Biomaterialia; 2011,7 (5), 2355-2373.

Available : <https://doi.org/10.1016/j.actbio.2011.03.016>

(Ratheesh,17) : G. Rathesh, J.R.Venugopal, A.Chinappan, H.Ezhilarasu, A.Sadiq, S.Ramakrishna; 3D Fabrication of polymeric scaffolds for regenerative therapy; ACS Biomaterial Science and Engineering; 2017, 3 (7), 1175-1194.

Available: <https://doi.org/10.1021/acsbiomaterials.6b00370>

(Saunders,14) : R.E.Saunders, B.Derby; Inkjet printing biomaterials for tissue engineering: bioprinting, International Materials Review; 2014, 59 (8), 430-448.

Available: <https://doi.org/10.1179/1743280414Y.0000000040>

(Selim,24) : M.Selim, H.M. Mousa, M.U.A.Khan, G.T.Abdel-Jaber, N.M.Mubarak, A. Barhoum, A.Al-Anazi, A.A-Hay; Enhancing 3D scaffold performance for bone tissue engineering: A comprehensive review of modification and functionalization strategies; Journal of Science: Advanced Materials and Devices; 2024, 9 (4), 100806.

Available: <https://doi.org/10.1016/j.isamd.2024.100806>

(Sharma,18) : S.K.Sharma, D.S.Verma, L.U.khan,S.Kumar, S.B.Khan; Chapter 10, Rare earth luminescence electronic spectroscopy and applications; Handbook of Materials and Characterization; 2018,345-404.

Available: <https://doi.org/10.1007/978-3-319-92955-2>

(Shanon,76): R.D.Shanon; Revised effective ionic radii and systematic studies of interatomic distance in halides and chalcogenides; Acta Crystallographica;1976, 32, 751-767.

Available: <https://doi.org/10.1107/S0567739476001551>

Shin-Etsu RE : Available: <https://www.rare-earth.jp/en/about.html> (Visited April 2025)

(Soderlund,15) : H.Soderlund, M.Mousavi, H.Liu, S, A.Engles; Increasing depth penetration in biological tissue imaging using 808nm excited Nd<sup>3+</sup>/Yb<sup>3+</sup>/Er<sup>3+</sup> -doped upconverting nanoparticles; Journal of Biomedical Optics; 2015, 20 (8), 86008.

Available: <https://doi.org/10.1117/1.jbo.20.8.086008>

(Stan,18) : C.V.Stan, C.M.Beavers, M.Kunj, N.Tamura; X-ray diffraction under extreme conditions at the advanced light source.; Quantum Beam science; 2018, 2 (1), 4.

Available: <https://doi.org/10.3390/qubs2010004>

(Stratton,16) : S. Stratton, N.B.Shelke, K.Hoshino, S.Rudraiah, S.G.Kumbar; Bioactive polymer scaffold for tissue engineering; Bioactive Materials; 2016, 1 (2), 98-108.

Available : <http://dx.doi.org/10.1016/j.bioactmat.2016.11.001>

(Szczođra,24.a) : A.Szczođra, A.Houaoui, T.Salminen, M.Hannula, V.A.Gobbo, S.Ghanvati, S.Miettinen, J. Massera; Pore-graded borosilicate bioactive glass scaffolds *in vitro* dissolution and cytocompatibility; Journal of Materials Science: Materials in Medicine; 2014, 35 (1),17.

Available: <https://doi.org/10.1007/s10856-024-06791-1>

(Szciodra,24 b) : A.Szciodra, A.Houaoui, R.Agniel, L. Sicard, S.Miettinen, J.Massera, C.Gorin; Boron Substitution in Silicate bioactive glass Scaffolds to enhance bone differentiation and regeneration, *Acta Biomaterialia*; 2024,186, 489-506.

Available:<https://doi.org/10.1016/j.actbio.2024.07.053>

(Thirumalai,16) : J. Thirumalai; Chapter 6: Photon upconverting materials: advances and prospects for various emerging applications; *Luminescence -An outlook on the phenomena and their applications*; 2016, 109-131.

Available:<https://doi.org/10.5772/62517>

(Tian,20) : Y.Tian, X.Li, R.Shen, C.Han. X.Wang, S.Xu. L.Cheng, J.Sun, J.Zhang, X.Zhang, B.Chen; Laser-induced thermal effect and the role of Nd<sup>3+</sup> in Tm<sup>3+</sup>/Yb<sup>3+</sup>/Nd<sup>3+</sup> triply doped LaNbO<sub>4</sub> up-conversion phosphors under 808 nm excitation; *Journal of Luminescence*; 2020, 223;117201.

Available:<https://doi.org/10.1016/j.jlumin.2020.117201>

(Trifanova,23) : E.M.Trifanova, G.Babayeva, M.A.Khvorostina, A.V. Atanova, M.E.Nikoeva, A.V.Sochilina, E.V.Khaydykov, V.K.Popov; Photoluminescent scaffolds based on natural and synthetic biodegradable polymers for bioimaging and tissue engineering; *Pharmaceutical Science*, MDPI; 2023, 13 (4), 870.

Available:<https://doi.org/10.3390/life13040870>

(Wang,15) : D.Wang, B.Xue, X.Kong, L.Tu, X.Liu, Y.Zhang, Y.Chang, Y.Luo, H.Zhao, H.Zhang; 808nm driven Nd<sup>3+</sup> sensitized upconversion nanostructures for photodynamic therapy and simultaneous fluorescence imaging, *Nanoscale Journal*; 2015, 7 (1), 190-197.

Available: <https://doi.org/10.1039/c4nr04953e>

(Wang, 22) : L.Wang, W.Yang, L.Li, S.Hu, M.Yuan, K.Han, H.Wang, X.Xu; Simultaneous Observation of Visible Upconversion and Near-Infrared Downconversion in SrF<sub>2</sub>:Nd<sup>3+</sup> /Yb<sup>3+</sup> /Er<sup>3+</sup> Nanocrystals and Their Application for Detecting Metal Ions under Dual-Wavelength Excitation, *ACS Omega*; 2022, 7 (31), 27230-27238.

Available:<https://doi.org/10.1021/acsomega.2c01968>

(Wang,23): L.Y.Wang, L.J.Chan, X.Zha et al; Infection Microenvironment mediated Nano-platform for *in vivo* persistent Luminescence imaging and chemodynamic antibacterial therapy, *ACS Applied Nano Materials*; 2023, 6 (3), 2274-2283.

Available:<https://doi.org/10.1021/acsanm.3c00101>

(Walters,11) : A.Walters, P.Lutsy; Rare earth elements; BGS Natural Environment Research Council ; 2011, 1-45 (Visited June,2025).

Available:

[https://nora.nerc.ac.uk/id/eprint/17448/1/Rare Earth Elements\\_profile%5B1%5D.pdf](https://nora.nerc.ac.uk/id/eprint/17448/1/Rare_Earth_Elements_profile%5B1%5D.pdf)

(Wing,18) : Z.Wing, A.Meijerink; Concentration Quenching in Upconversion Nanocrystals; The journal of physical chemistry; 2018, 122 (45), 25709-26306.

Available:<https://doi.org/10.1021/acs.jpcc.8b09371>

(Xing,13) : L.Xing, Y.Xu, R.Wang, W.Xu, Z.Zhang; Highly sensitive optical thermometry based on upconversion emissions in  $Tm^{3+}/Yb^{3+}$  co-doped  $LiNbO_3$  single crystal, Optical Letters;2013, 39 (3), 454-457.

Available: <https://doi.org/10.1364/OL.39.000454>

(Xu,19) : J.Xu, S.Tanabe; Persistent Luminescence instead of phosphorescence: History, mechanism and perspective; Journal of Luminiscence; 2019, 205, 581-620.

Available: <https://doi.org/10.1016/j.jlumin.2018.09.047>

(Yang,24) : J.Yang, Y. Wang, Y.Yang, X.Su, Z.Xu, Y. Hu, J.Lai, H.Zhou, C.Dai, Z.A.Li, L.Qin, N.Hu; 3D printed bioactive scaffolds: an emerging strategy for the regeneration of infectious bone defects; International Journal of Bioprinting; 2024, 11 (2), 79-138.

Available: <https://doi.org/10.36922/ijb.4986>